SCIENCE CHINA
Technological Sciences

Special Issue: Celebrating the 70th Anniversary of School of Mechanical Science and Engineering of HUST
•Review•

September 2022 Vol.65 No.9: 2007–2030
https://doi.org/10.1007/s11431-022-2090-4

Advanced Mueller matrix ellipsometry: Instrumentation and emerging applications

CHEN XiuGuo[1,2*], GU HongGang[1,2*], LIU JiaMin[1,2], CHEN Chao[1,2] & LIU ShiYuan[1,2*]

[1] *State Key Laboratory of Digital Manufacturing Equipment and Technology, Huazhong University of Science and Technology, Wuhan 430074, China;*
[2] *Optics Valley Laboratory, Wuhan 430074, China*

Received April 6, 2022; accepted May 20, 2022; published online August 15, 2022

Mueller matrix ellipsometry (MME) provides the 4×4 Mueller matrix of a sample under test, which determines how the state of polarization is changed as light interacts with the sample. Due to the redundant information contained in the Mueller matrix, MME has gained more and more extensive applications in the characterization of surfaces, interfaces, thin films, and nanostructures. In addition, the instrumentation of MME has also achieved great developments since its advent in the 1970s. In this paper, we will first review the basic principle as well as the common system layouts of MME for the full Mueller matrix measurement. Then, the basic procedure of ellipsometry data analysis is reviewed. After that, some new developments in MME in our lab for different applications are introduced, including the broadband MME, the high-resolution imaging MME, and the high-speed MME. Some emerging applications of the developed MMEs are also presented. Conclusions and perspectives of the advanced ellipsometry are finally drawn and discussed.

ellipsometry, Mueller matrix, Mueller matrix ellipsometry, imaging ellipsometry, high-speed ellipsometry

Citation: Chen X G, Gu H G, Liu J M, et al. Advanced Mueller matrix ellipsometry: Instrumentation and emerging applications. Sci China Tech Sci, 2022, 65: 2007–2030, https://doi.org/10.1007/s11431-022-2090-4

1 Introduction

Ellipsometry has a history of more than 100 years from its birth to its development [1,2]. The German scientist Drude [3] is the founder of ellipsometry. He derived the well-known ellipsometry equation in 1887 and first developed the null ellipsometry device (a prototype of the ellipsometer) in 1901. In 1945, Rothen [4] coined the concept of "ellipsometer" for the first time in the world. Due to the limitations in the measurement efficiency and accuracy of the ellipsometer instrument, the early research on the ellipsometry mainly focused on the theory of polarized light, the optical design of the instrument itself, and the physics of the interaction between polarized light and materials. Since the 1960s, with the rapid development of computer technology and the continuous progress of optical technology, the measurement efficiency and accuracy of the ellipsometer have been greatly improved. Various principles and configurations of ellipsometers [5], such as the rotating-polarizer (or rotating-analyzer) ellipsometer and the rotating-compensator ellipsometer, have been developed. Ellipsometry has gradually become the de facto standard tool for characterizing the thickness of thin-film materials and their optical properties [6–11].

As a kind of advanced ellipsometry, the Mueller matrix ellipsometry (MME) was first developed by Azzam [12] in 1978. By controlling the two retarders on the polarization state generator (PSG) and the polarization state analyzer (PSA) to rotate synchronously at a rotation ratio of 5:1, the

*Corresponding authors (email: xiuguochen@hust.edu.cn; hongganggu@hust.edu.cn; shyliu@hust.edu.cn)

© Science China Press and Springer-Verlag GmbH Germany, part of Springer Nature 2022

instrument can obtain a 4 × 4 Mueller matrix under the measurement conditions of each wavelength and each incident angle. Since MME provides more abundant measurement information such as sample anisotropy and depolarization than traditional ellipsometry, it has quickly been used in the characterization of various surfaces, interfaces, thin films, and sub-wavelength nanostructures [13–16]. The recent development of MME has also witnessed its application in the field of biomedical material characterization and clinical disease diagnosis [17–19].

With the rapid development of modern nanoscience and nanotechnology, many new materials are emerged, such as two-dimensional (2D) materials [20] and organic materials for the organic photovoltaic (OPV) and organic light emitting diode (OLED) [21]. The accurate characterization of optical properties of these new materials is the foundation for the analysis and design of optoelectronics devices using these materials. Considering that the bandgaps of these new materials may appear in the ultraviolet (UV), visible (VIS) or infrared (IR) spectrum, we have developed a broadband MME covering the UV-VIS-IR spectrum to characterize these new materials [22]. Although traditional spectroscopic ellipsometry (SE) has very high thickness sensitivity (–0.1 Å) [8], its lateral resolution is totally determined by its illumination spot size, which restricts its application in the characterization of thin-film materials and nanostructures located in micro-regions, such as the mechanically exfoliated 2D materials and the pixelated nanogratings used for three-dimensional (3D) holographic display. To this end, we have further developed a high-resolution imaging MME (IMME) by combing the developed MME with the microscopic imaging technique [23,24]. The developed IMME allows for the direct visualization of the sample under test and intuitive selection of regions of interest for ellipsometry analysis with sub-micron resolution. In addition, some high-speed dynamic physical and chemical processes, such as the alignment and ordering of liquid crystal molecules under an applied electric field, often only occur in microseconds or even sub-microseconds. To acquire and characterize the transient light-matter interactions, we have also further developed a high-speed MME with microsecond temporal resolution [25].

In this paper, we will review the instrumentation and applications of the above three kinds of MMEs developed in our lab during the past years, as summarized in Figure 1. We first introduce the basic principles of Mueller matrix ellipsometry in Sect. 2, and summarize the existing common system layouts of full Mueller matrix measurement. Then we introduce the basic procedure of ellipsometry data analysis. In Sect. 3, we will introduce the principles and instrumentation of the developed broadband MME, high-resolution IMME, and high-speed MME in our lab. With the developed instruments, some emerging applications are presented in Sect. 4, including the characterization of 2D materials, organic materials, and dynamic optical properties, and metrology of nanostructures. Finally, the work of the full paper is summarized and prospected.

2 Basic principle

2.1 Principles of Mueller matrix measurement

Figure 2 depicts the basic system layout of a Mueller matrix ellipsometer, which is typically composed of a light source, a detector, a PSG and a PSA. The PSG and PSA are typically composed of identical polarization components such as polarizers (or analyzers) and retarders (also called compensators) but are arranged in a reverse order. The PSG generates a set of Stokes vectors $\mathbf{S}_j$ ($j = 1, 2, \ldots, N$; $N \geq 4$) incident upon a sample with a Mueller matrix of $\mathbf{M}$. The output Stokes vectors $\mathbf{MS}_j$ are then analyzed by a set of analyzer vectors $\mathbf{A}_i$ ($i = 1, 2, \ldots, M$; $M \geq 4$) generated by the PSA. This process finally leads to a set of fluxes g_{ij} that can be measured by the detector. Note that here both $\mathbf{S}_j$ and $\mathbf{A}_i$ are 4 × 1 column vectors. Mathematically, the above scheme can be represented as

$$g_{ij} = \mathbf{A}_i^{\mathrm{T}}\mathbf{M}\mathbf{S}_j, \tag{1}$$

or in a matrix form as

$$\mathbf{G} = \mathbf{AMS}, \tag{2}$$

where

$$\mathbf{G} = \begin{bmatrix} g_{11} & g_{12} & \cdots & g_{1N} \\ g_{21} & g_{22} & \cdots & g_{2N} \\ \vdots & \vdots & \ddots & \vdots \\ g_{M1} & g_{M2} & \cdots & g_{MN} \end{bmatrix}, \tag{3}$$

$$\mathbf{A} = \begin{bmatrix} \mathbf{A}_1^{\mathrm{T}} \\ \mathbf{A}_2^{\mathrm{T}} \\ \vdots \\ \mathbf{A}_M^{\mathrm{T}} \end{bmatrix}, \tag{4}$$

$$\mathbf{S} = \begin{bmatrix} \mathbf{S}_1 & \mathbf{S}_2 & \cdots & \mathbf{S}_N \end{bmatrix}. \tag{5}$$

To obtain the full Mueller matrix $\mathbf{M}$, the matrices $\mathbf{A}$ and $\mathbf{S}$ are required to be full rank matrices, and rank($\mathbf{A}$) = rank($\mathbf{S}$) = 4, where rank(·) denotes the matrix rank. According to eq. (2), the sample Mueller matrix $\mathbf{M}$ can be obtained as

$$\mathbf{M} = \mathbf{A}^{+}\mathbf{G}\mathbf{S}^{+}, \tag{6}$$

where $\mathbf{A}^{+} = (\mathbf{A}^{\mathrm{T}}\mathbf{A})^{-1}\mathbf{A}^{\mathrm{T}}$ and $\mathbf{S}^{+} = \mathbf{S}^{\mathrm{T}}(\mathbf{S}\mathbf{S}^{\mathrm{T}})^{-1}$ are the left and right pseudo-inverses of matrices $\mathbf{A}$ and $\mathbf{S}$, respectively, which are also called the Moore-Penrose pseudo-inverse. In the case of $\mathbf{A}$ and $\mathbf{S}$ being full rank square matrices, $\mathbf{A}^{+} = \mathbf{A}^{-1}$ and $\mathbf{S}^{+} = \mathbf{S}^{-1}$. Eq. (2) can also be solved using the vectorization operator. Taking the vectorization of both sides of eq. (2) leads to

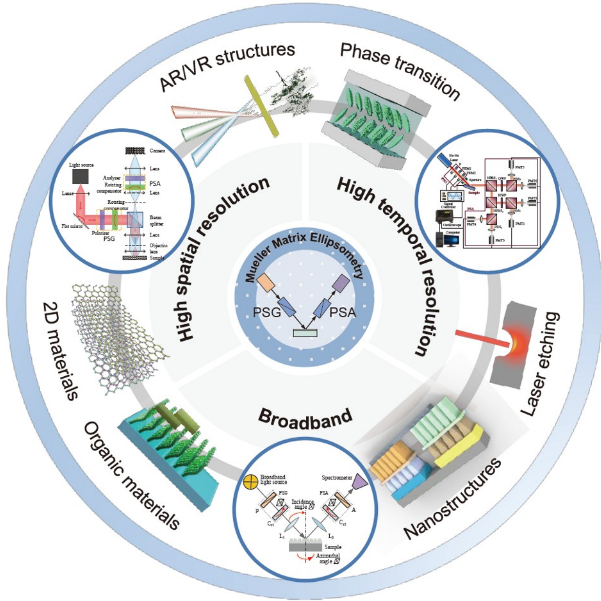

Figure 1 (Color online) Summary of the research work in our lab on the instrumentation and emerging applications of MME.

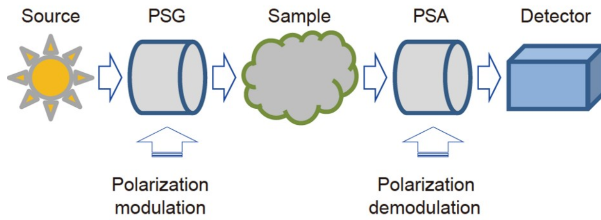

Figure 2 (Color online) Basic principle of the Mueller matrix measurement.

$$\mathrm{vec}(\mathbf{G}) = (\mathbf{S}^{\mathrm{T}} \otimes \mathbf{A})\mathrm{vec}(\mathbf{M}) \equiv \mathbf{D}\mathrm{vec}(\mathbf{M}), \tag{7}$$

where vec(·) denotes the vectorization operator, which converts a matrix into a column vector in a lexicographic order. For instance, $\mathrm{vec}(\mathbf{M}) = [M_{11}, M_{21}, M_{31}, M_{41}, M_{12}, M_{22}, \ldots, M_{34}, M_{44}]^{\mathrm{T}}$. According to eq. (7), it follows that

$$\mathrm{vec}(\mathbf{M}) = \mathbf{D}^{+}\mathrm{vec}(\mathbf{G}), \tag{8}$$

where $\mathbf{D}^{+}$ denotes the Moore-Penrose pseudo-inverse of the matrix **D**. The latter is also called the instrument matrix, which is determined by the system parameters of the instrument, including the orientation angles of transmission axes of the polarizer and analyzer, the orientation angles of fast axes and phase retardances of the compensators, as well as the polarization parameters of other optical components in the optical path that may change polarization states, such as beamsplitters and high numerical aperture (NA) objective lenses. The purpose of instrument calibration is to acquire the true value of the instrument matrix. In addition, the condition number of the instrument matrix, i.e.,

$$\mathrm{cond}(\mathbf{D}) = \|\mathbf{D}\|_p \, \|\mathbf{D}^{+}\|_p, \tag{9}$$

is usually adopted to optimize the system parameters of the instrument to achieve more precise Mueller matrix measurement [26–28]. Here, the notation $\|\mathbf{D}\|_p$ denotes the p-norm of **D**, and p can be 1, 2, or ∞.

Eq. (8) describes the general principle of sample Mueller matrix measurement for any type of Mueller matrix ellipsometers. According to eq. (2), we know that the PSG needs to generate at least 4 linearly independent Stokes vectors $\mathbf{S}_j$ and simultaneously PSA needs to generate at least 4 linearly independent analyzer vectors $\mathbf{A}_i$ to obtain the full sample Mueller matrix **M**. Many polarization modulation and demodulation techniques have been developed to generate 4 linearly independent Stokes vectors $\mathbf{S}_j$ and 4 linearly independent analyzer vectors $\mathbf{A}_i$ over the past decades. In summary, these techniques can be classified overall into three categories, namely, the temporal polarization-coding approach, the spectral polarization-coding approach, and the spatial polarization-coding technique. Table 1 [29–34] summarizes the characteristics of the common instruments for full Mueller matrix measurement.

In the temporal polarization-coding technique, the approaches to realizing polarization modulation and demodulation can be further divided into two categories. The first approach is to change the orientations of fast axes of the compensators continuously and discretely over time, such as the dual rotating-compensator MME (DRC-MME) [12,35,36] and the MME with four ferroelectric liquid crystals (4-FLC MME) [33,34,37]. In the DRC-MME, the two compensators (one is in the PSG and another one is in the PSA) rotate synchronously with a rotation speed of typically 5:1 and 5:3. In the 4-FLC MME, both PSG and PSA have two FLCs and the fast axis of each FLC can be electrically switched between two orientations separated 45° from each other. The second approach is to adjust the retardances of the compensators with the orientations of their fast axes fixed, such as the MME with four liquid-crystal variable retarders (4-LCVR MME) [38–40], with four Pockels-cell modulators (4-PCM MME) [41], or with four photoelastic modulators (4-PEM MME) [42]. The system layouts of the second approach are similar, where both PSG and PSA contain two retarders. However, the LCVR has a voltage-controlled retardance, typically in a square wave form with respect to the driver rms voltage, while the retardances of PCM and PEM are electrically driven and vary sinusoidally with time at frequencies of several or several tens of kHz.

The spectral polarization-coding approach relies on a property that the retardances of some multi-order birefringent crystals, such as quartz, MgF_2, calcite and sapphire, change approximately linearly with wavenumber in a limited wave band. The above multi-order birefringent retarders encode polarization information into the intensity spectrum, and by performing Fourier analysis we can recover

Table 1 Advantages and disadvantages of instruments for full Mueller matrix measurement

Instrument types	Advantages	Disadvantages
DRC-MME	Fast Mueller matrix measurement in a broad spectral range from vacuum-UV to near-IR (several seconds), spectrum to the mid-IR or even the terahertz is also possible [29–31] High stability (less sensitive to ambient temperature)	Contain rotating elements, which may introduce beam wandering due to imperfect compensators Specially designed achromatic compensators Complex calibration procedure
4-FLC MME	Fast Mueller matrix measurement in a broad spectral range from VIS to near-IR (several seconds) No rotating elements in measurement	Specially designed FLCs for broadband measurement, e.g., a quarter waveplate or another FLC is introduced between the two FLCs in both PSG and PSA [33,34] Temperature sensitive retarder
4-LCVR MME	Retardance can be adjusted on demand Well suited for Mueller matrix measurement at discrete wavelengths, such as imaging MME No rotating elements in measurement	Long time for broadband measurement (several or several tens of minutes) Temperature sensitive retarder Similar to FLC, UV band is also infeasible
4-PCM/4-PEM MME	Fast Mueller matrix measurement at a single wavelength (several or several tens of microseconds) Broad spectral range from vacuum-UV to near-IR for PEM No rotating elements in measurement	Long time for broadband measurement (several or several tens of minutes) Temperature sensitive retarder Complex calibration procedure
Snapshot MME	Fast Mueller matrix measurement (could reach 10 ns according to a latest report [32]) No rotating or active elements in measurement Compact size	Limited wave band, typically less than 100 nm Low measurement accuracy due to the inherent low-pass filtering property Temperature sensitive retarder

the polarization parameters from the modulated spectrum [43]. The full Mueller matrix measurement is realized by employing four multi-order birefringent waveplates (two in the PSG and another two in the PSA) with a proper thickness ratio and with the orientations of their fast axes fixed at proper angles. The commonly adopted thickness ratios of the four multi-order birefringent waveplates include 1:2:5:10, 1:1:5:5, and 1:4:2:9 [44–46]. Since complete measurements can be realized in a single integration interval of the spectrometer, without rotating or active elements, the spectral polarization-coding approach is usually called the snapshot Mueller matrix measurement.

In the spatial polarization-coding approach, the polarization information is encoded and decoded at different spatial locations. As a kind of spatial polarization-coding approaches, the division-of-wavefront (DoW) technqiue [47], which is usually adopted in polarimetric measurements, divides the wavefront into different parts (using such as a micropolarzer array) and each part corresponds to a different polarization states. Simultaneous measurement of the Stokes vector elements is then realized by analyzing the polarization modulated wavefront. Note that the counterpart of DoW for simultaneous measurement of Stokes vector elements, the division-of-amplitude (DoA) technqiue [48,49], where the entire wavefront of the light beam is successively split to achieve polarization modulation, can be regarded as a temporal polarization-coding approach. Ref. [50] reported the development of a so-called rapid Mueller matrix polarimetry (RAMMP) based on the spatial polarization-coding approach. In the RAMMP, spatially distributed polarization states are achieved on the back focal plane of a microscope objective via vectorial beams. However, it is noted that RAMMP can only extract twelve of the sixteen Mueller matrix elements. So far, there is no configuration yet that could truly realize complete Mueller matrix measurement with the spatial polarization-coding technique.

2.2 Data analysis

Figure 3 presents the basic procedure of the ellipsometry data analysis. In this procedure, an optical model corresponding to the sample under measurement is constructed first. For a thin film sample, a multi-layer film model can be constructed according to the optical property of each film layer, and each layer is characterized by its film thickness and optical constants. If the film sample contains a grating structure, the profile of the grating structure should be parameterized according to prior knowledge. After that, the optical constants of each layer at different incident wavelengths are selected by look-up table. However, when the optical constants are not known, a proper dielectric function is required to model the optical property of the associated layer. The dielectric function describes how the material's optical properties are varied with the incident wavelengths. Many dielectric function models have been developed up to now [7–11], which can be selected according to the prior knowledge about material's optical properties. For instance, the Cauchy and Sellmeier models are used to describe transparent materials. The Lorentz, Harmonic, and Gaussian models describe a resonant absorption, while the Drude model describes a free-carrier absorption.

After the construction of the optical model and the dielectric function models, the ellipsometric spectra can be calculated. For isotropic multi-layer films, the 2×2 transfer matrix method [51] can be adopted to calculate the ellipsometric parameters. If the film sample contains anisotropic

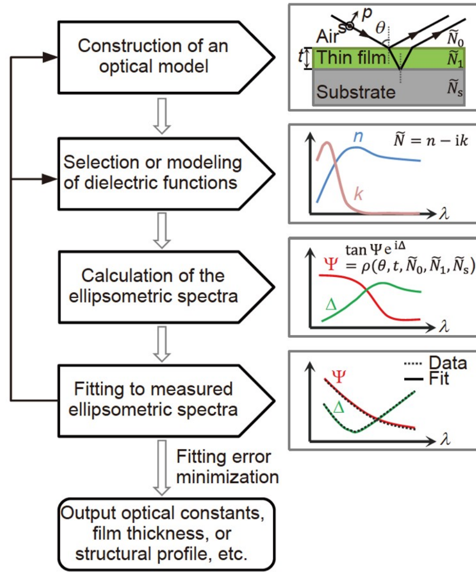

Figure 3 (Color online) Flowchart of the ellipsometry data analysis.

materials, the Berreman's 4×4 matrix method [51] should be used to calculate the ellipsometric data. If the film sample contains a grating structure, the rigorous coupled-wave analysis method (RCWA, also named as Fourier modal method) [52] is typically applied to calculate the sample's optical response. According to the above mentioned calculation methods, we can obtain the sample Jones matrix $\mathbf{J}$, which connects the incoming Jones vector with the reflected (or transmitted) Jones vector by

$$\begin{bmatrix} E_{rp} \\ E_{rs} \end{bmatrix} = \begin{bmatrix} r_{pp} & r_{ps} \\ r_{sp} & r_{ss} \end{bmatrix} \begin{bmatrix} E_{ip} \\ E_{is} \end{bmatrix} \equiv \mathbf{J} \begin{bmatrix} E_{ip} \\ E_{is} \end{bmatrix}, \tag{10}$$

where E_{sp} refers to the electric field component perpendicular and parallel to the plane of incidence, respectively. For isotropic samples, the cross-polarization components in the Jones matrix equal zero, i.e., $r_{ps} = r_{sp} = 0$, the traditional ellipsometric parameters can be obtained by

$$\rho = \frac{r_{pp}}{r_{ss}} \equiv \tan\Psi \exp(\mathrm{i}\Delta), \tag{11}$$

where Ψ and Δ represent the amplitude-ratio and phase-difference angles, respectively. In the absence of depolarization, the sample Mueller matrix $\mathbf{M}$ can be obtained from the Jones matrix by

$$\mathbf{M} = \begin{bmatrix} M_{11} & M_{12} & M_{13} & M_{14} \\ M_{21} & M_{22} & M_{23} & M_{24} \\ M_{31} & M_{32} & M_{33} & M_{34} \\ M_{41} & M_{42} & M_{43} & M_{44} \end{bmatrix} = \mathbf{U}(\mathbf{J} \otimes \mathbf{J}^*)\mathbf{U}^{-1}, \tag{12}$$

where $\otimes$ denotes the matrix Kronecker product, $\mathbf{J}^*$ denotes the complex conjugate of $\mathbf{J}$, and the matrix $\mathbf{U}$ is given by

$$\mathbf{U} = \begin{bmatrix} 1 & 0 & 0 & 1 \\ 1 & 0 & 0 & -1 \\ 0 & 1 & 1 & 0 \\ 0 & \mathrm{i} & -\mathrm{i} & 0 \end{bmatrix}. \tag{13}$$

In practice, the Mueller matrix elements are usually normalized to the M_{11} element to makes all the element values within the range of $[-1,1]$. For isotropic samples, the Mueller matrix elements are simplified to be $M_{11} = M_{22} = 1$, $M_{12} = M_{21} = -\cos(2\Psi)$, $M_{33} = M_{44} = \sin(2\Psi)\cos\Delta$, and $M_{34} = -M_{43} = \sin(2\Psi)\sin\Delta$, with the elements of the two 2×2 off-diagonal blocks M_{ij} ($i, j = 3, 4$) being zero. However, for the general anisotropic samples, all the Mueller matrix elements will no longer be zero.

The least-squares regression analysis is then performed, during which the measurands are adjusted until the calculated and the measured ellipsometric spectra match as close as possible. In the regression analysis, the constructed optical model will be calculated several times in each iteration (equal to the number of measurands in the gradient-based optimization algorithms), which leads to the fitting procedure time-consuming and hence restricts the use of the regression analysis method for in-line applications, especially for grating samples with complex structural profiles. In this case, the library search method can be adopted, where an ellipsometric spectra library is generated offline prior to the experiment and then the library is searched to find the best match with the measured spectra [53]. Alternatively, an artificial-neural-network-based surrogate electromagnetic solver mapping from measurands to ellipsometric spectra can also be used to calculate the ellipsometric spectra in the regression analysis to accelerate the fitting procedure [54]. In the above approaches, the solution of the measurands is achieved by minimizing a χ_r^2 merit function, which in terms of Mueller matrix elements can be expressed as

$$\chi_r^2 = \frac{1}{15N_\lambda - P} \sum_{l=1}^{N} \sum_{i,j=1}^{4} \frac{\left[M_{ij,l}^{meas} - M_{ij,l}^{calc}(\mathbf{x})\right]^2}{\sigma^2(M_{ij,l})}, \tag{14}$$

where i and j are the indices for the Mueller matrix elements, l indicates the l-th spectral point from total number N_λ, $\mathbf{x}$ is a P-dimensional vector comprised of the measurands, $M_{ij,l}^{meas}$ and $M_{ij,l}^{calc}$ represent the measured and calculated Mueller matrix elements, respectively, and $\sigma^2(M_{ij,l})$ is the variance associated with $M_{ij,l}$. The fitting procedure also delivers confidence limits for the measurands. The 95% confidence limit for the m-th measurand ($m = 1, 2, \ldots, P$) is given by $1.96 \times \chi_r \times \sqrt{C_{mm}}$, where C_{mm} is the m-th diagonal element of the covariance matrix of the fit parameters [55].

It should be noted that the finding of the measurands is not the end-all of the fitting procedure. To guarantee a reasonable output, the fit results should be evaluated at least from the following three aspects. First, the fitting error between the

measured and calculated best-fit ellipsometric spectra. Although a small fitting error does not necessarily guarantee reasonable fit parameters, a relatively large fitting error indicatively requires an improvement of the constructed optical model or the selected dielectric function models. Second, error or uncertainty estimates (according to the covariance matrix of the fit parameters) on the measurands. A large estimated uncertainty of a measurand typically indicates a low measurement sensitivity to the corresponding measurand or a large correlation with respect to other measurands. In this situation, it is recommended to fix the corresponding measurand in the fitting procedure. Third, physical realizability of the fit parameters, which means that the fit parameters must be physical. For example, the imaginary part of the complex refractive index (i.e., the extinction coefficient k; the real part of the complex refractive index corresponds to the common refractive index n) must always be non-negative. The real and imaginary parts of physically correct complex dielectric constants (the complex dielectric constant is the square of the complex refractive index) should follow the Kramers-Kronig relations [7,8]. In addition, since ellipsometry is inherently an indirect measurement, all fit parameters are deduced from the collected ellipsometric spectra based on a constructed optical model, other complementary characterization techniques, such as atomic force microscopy (AFM), scanning electron microscopy (SEM), Raman spectroscopy, and stylus profilometry, are recommended to be used to collaborate and evaluate the analysis results by ellipsometry.

3 Instrumentation

3.1 Broadband Mueller matrix ellipsometer

Compared with other types of MME, as described in Sect. 2.1, the DRC-MME can realize fast Mueller matrix measurement in a broad spectral range and has a high temperature stability. We have developed a broadband DRC-MME [22]. Figure 4(a) depicts the basic system layout of the developed DRC-MME, where the orientation angles of fast axes of the 1st and 2nd compensators rotate synchronously at $\omega_1 = 5\omega$ and $\omega_2 = 3\omega$, with ω being the fundamental mechanical frequency. The Stokes vector $\mathbf{S}_{\text{out}}$ of the exiting light beam can be expressed as the following Mueller matrix product:

$$\mathbf{S}_{\text{out}} = \mathbf{M}_{\text{P}}(\phi_{\text{A}}) \cdot \mathbf{M}_{\text{C}}(\delta_2, \phi_{\text{C2}}) \cdot \mathbf{M}_{\text{S}} \cdot \mathbf{M}_{\text{C}}(\delta_1, \phi_{\text{C1}}) \cdot \mathbf{M}_{\text{P}}(\phi_{\text{P}}) \cdot \mathbf{S}_{\text{in}}, \tag{15}$$

where $\mathbf{M}_{\text{P}}(\phi) = \mathbf{R}(-\phi)\cdot\mathbf{M}_{\text{P}}\cdot\mathbf{R}(\phi)$ and $\mathbf{M}_{\text{C}}(\delta, \phi) = \mathbf{R}(-\phi)\cdot\mathbf{M}_{\text{C}}(\delta)\cdot\mathbf{R}(\phi)$, with $\mathbf{M}_{\text{P}}$ and $\mathbf{M}_{\text{C}}(\delta)$ being the Mueller matrices of the polarizer (or analyzer) and compensator, respectively, and $\mathbf{R}(\phi)$ being the Mueller transformation matrix for rotation by an angle ϕ, which can be orientation angles of transmission axes of the polarizer and analyzer, ϕ_{P} and ϕ_{A}, or orientation angles of fast axes of the 1st and 2nd compensators, ϕ_{C1} and ϕ_{C2}, δ_1 and δ_2 are the phase retardances of the two compensators, and $\mathbf{M}_{\text{S}}$ is the sample Mueller matrix. By multiplying the matrices in eq. (15), the light intensity collected by the detector can be expressed as [36]

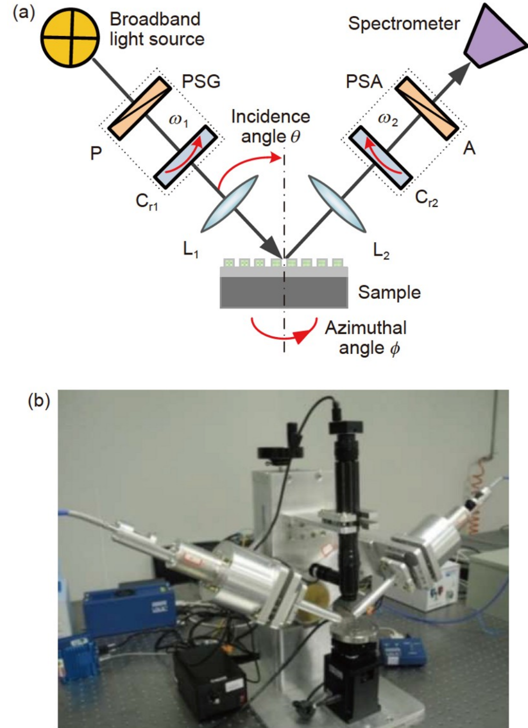

Figure 4 (Color online) (a) System layout and (b) prototype of the developed broadband DRC-MME, adapted from ref. [22]. P and A, polarizer and analyzer; C_{r1} and C_{r2}, the 1st and 2nd rotating-compensators; L_1 and L_2, focusing and collecting lenses, which can be removable in measurement.

$$\begin{aligned} I(t) &= I_{00}M_{11}\left\{a_0 + \sum_{n=1}^{16}\left[a_{2n}\cos(2n\omega t - \phi_{2n}) + b_{2n}\sin(2n\omega t - \phi_{2n})\right]\right\}, \\ &= I_0\left\{1 + \sum_{n=1}^{16}\left[\alpha_{2n}\cos(2n\omega t - \phi_{2n}) + \beta_{2n}\sin(2n\omega t - \phi_{2n})\right]\right\}, \end{aligned} \tag{16}$$

where I_{00} is the spectral response function, ϕ_{2n} is the angular phase shift, $I_0 = I_{00}M_{11}a_0$, $\alpha_{2n} = a_{2n}/a_0$ and $\beta_{2n} = a_{2n}/a_0$ are the d.c. and d.c.-normalized a.c. harmonic coefficients, respectively. The sample Mueller matrix elements M_{ij} (i, j = 1, 2, 3, 4) are linear combinations of α_{2n} and β_{2n}. Further details about the relation between M_{ij} and α_{2n} and β_{2n} are given in ref. [36]. According to these combinations, the sample Mueller matrix elements can be finally obtained from these harmonic coefficients.

To realize Mueller matrix measurements in a broad spectral range, a key step is to design a compensator that can realize achromaticity in a broadband. In addition, according to the optimization result based on the condition number of the instrument matrix, i.e., cond($\mathbf{D}$), the optimal phase re-

tardance δ of the two compensators is about 130° [56,57] (actually, there is no distinct variation in cond(**D**) when δ is within the range of [110°,150°]). It is therefore suggested that the two compensators in the DRC-MME are not the commonly used half waveplate or quarter waveplate, but a specially designed retarder that is better to keep a phase retardance of about 130° or within [110°,150°] over the whole spectral range.

A novel framework of composite waveplate is proposed to achieve super-achromatic compensator for broadband DRC-MME, in which both the central wavelengths (i.e., the thicknesses) and axis orientations of the single-waveplates are flexible parameters to be optimized, as shown in Figure 5. Compared with conventional designs where the single-waveplates are usually arranged in symmetrical layout or with their fast axes parallel or perpendicular to each other, the proposed framework of composite waveplate can provide approximately twice as many degrees of freedom to accommodate the optimization of the broadband MME. The structure of the proposed compensator, namely the central wavelengths λ and fast axis azimuths ϕ of the single-waveplates, are determined by minimizing the maximum condition number of the instrument matrix over the concerned wavelength range, as described by [57]

$$(\lambda_o, \phi_o) = \mathrm{argmin}[\max|\kappa(\lambda, \phi)|], \tag{17}$$

where λ_o and ϕ_o refer to the optimal values of the central wavelengths and orientations of fast axes of the single-waveplates, and $\kappa(\lambda, \phi)$ = cond(**D**). Finally, the optimized compensator based multi-waveplates can be fabricated and aligned accurately by comprehensively characterizing its full polarization features [58,59], and the residual errors in axis alignment and axis tilt can be evaluated and calibrated [60–62].

Instrument calibration is another key step to guarantee accurate Mueller matrix measurements in a broad spectral range. For a basic DRC-MME, the system parameters that need to be calibrated typically include the orientation angles of transmission axes of the polarizer and analyzer, ϕ_P and ϕ_A,

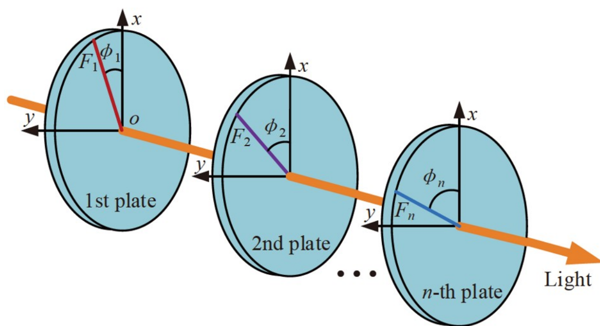

Figure 5 (Color online) Schematic of a general composite waveplate, adapted from ref. [57]. (F_i, ϕ_i) refer to the fast axis of the i-th single-waveplate and its orientation angle with respect to the x-axis, respectively.

the initial orientation angles of fast axes of the 1st and 2nd compensators, ϕ_{10} and ϕ_{20} (Note that $\phi_{C1} = \omega_1 t + \phi_{10}$ and $\phi_{C2} = \omega_2 t + \phi_{20}$), as well as the phase retardances δ_1 and δ_2 of the two compensators. To do this, we propose a nonlinear regression method to obtain the calibration values of the above system parameters. First, a calibration sample such as a standard SiO_2/Si film sample with a nominal film thickness of t is measured by the instrument at the incidence angle of θ. The measured normalized harmonic coefficients given in eq. (16) are denoted as $\alpha_{2n}^{\mathrm{meas}}$ and $\beta_{2n}^{\mathrm{meas}}$. Then, data calculated for the calibration sample, denoted as $\alpha_{2n}^{\mathrm{calc}}(\phi_P, \phi_A, \phi_{10}, \phi_{20}, \delta_1, \delta_2, t, \theta)$ and $\beta_{2n}^{\mathrm{calc}}(\phi_P, \phi_A, \phi_{10}, \phi_{20}, \delta_1, \delta_2, t, \theta)$, are fitted to the experimental data wavelength-by-wavelength by adjusting the fit parameters to minimize a χ^2 error function defined as

$$\chi^2 = \sum_{n=1}^{16}\left\{\left[\frac{\alpha_{2n}^{\mathrm{meas}} - \alpha_{2n}^{\mathrm{calc}}(\phi_P, \phi_A, \phi_{10}, \phi_{2n}, \delta_1, \delta_2, t, \theta)}{\sigma(\alpha_{2n})}\right]^2 + \left[\frac{\beta_{2n}^{\mathrm{meas}} - \beta_{2n}^{\mathrm{calc}}(\phi_P, \phi_A, \phi_{10}, \phi_{2n}, \delta_1, \delta_2, t, \theta)}{\sigma(\beta_{2n})}\right]^2\right\}, \tag{18}$$

where $\sigma(\alpha_{2n})$ and $\sigma(\beta_{2n})$ are the standard deviations of the measured harmonic coefficients. After obtaining the calibration values in the whole spectral range, we can further parameterize the calibrated system parameters with respect to the wavelengths, especially the phase retardances δ_1 and δ_2, using proper dielectric function models. According to the parameterized model, we may perform a similar χ^2 fitting procedure again for the whole spectral range to mitigate the impact of experimental noise on the prior calibration values.

Figure 4(b) presents the prototype of our developed broadband DRC-MME. The light source is a deuterium and quartz-tungsten-halogen combined source (B&W Tek, USA). The polarizer and analyzer are α-BBO Rochon prisms (Union Optic, Inc., China). Two optimally designed quartz triplates (cooperated with Union Optic) are employed as the compensators, which are mounted on hollow shaft motors and rotated synchronously with angular speeds of 12.5π and 7.5π rad/s, respectively. The detector is a custom-made spectrometer from B&W Tek with a spectral resolution of 0.5 nm. The sample Mueller matrix can be collected within a spectral range of 200–1000 nm within about 1 s. A focusing lens and a collecting lens are installed (removable) in the PSG and PSA, respectively, for micro-spot measurements (with a spot size of less than 200 μm). Figure 6 presents the estimated mean bias and standard deviation of the Mueller matrix elements from 30 repeated measurements on air (whose Mueller matrix is a 4-by-4 identity matrix as known) by the home-made DRC-MME in 200–1000 nm. As can be observed, the developed DRC-MME has a measurement accuracy better than 0.2% and a measurement precision better than 0.1% over the whole spectral range. Other test

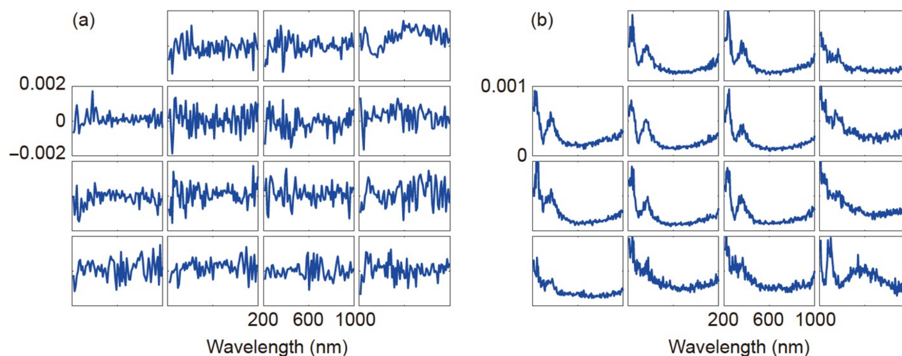

Figure 6 (Color online) (a) Mean bias and (b) standard deviation of the Mueller matrix elements estimated from 30 repeated measurements in the straight-through mode by the home-made DRC-MME in the spectral range of 200–1000 nm. Adapted from ref. [57].

results including experiments on a series of standard SiO_2/Si films can be found in ref. [57]. Now, the developed DRC-MME has been commercialized in cooperation with Wuhan EOptics, Inc. (www.eoptics.com.cn).

3.2 High-resolution imaging Mueller matrix ellipsometer

The lateral resolution of traditional SE is determined by its illumination spot in measurement. Standard spot sizes in traditional SE are in the range from 3 to 1 mm in diameter, and micro-spot sizes, depending on the spectral range of measurements, are typically between 50 and 25 μm due to the restriction of dispersion effects of optical components. The fit parameters obtained from ellipsometry data analysis are actually the averaged results of the sample over the illumination spot. When the sample under test is inhomogeneous over the illumination spot or the sample size is smaller than the spot size, the above average analysis will inevitably yield incorrect results.

Imaging ellipsometry is a hybrid of traditional SE and optical microscopy, which combines the strengths of the high thickness sensitivity of SE and the high spatial resolution of optical microscopy. Imaging ellipsometry techniques first emerged in the 1980s, which were developed for quantitative analysis of film thickness uniformity in semiconductor integrated circuit processing [63–67]. Over the past decades, many types of imaging ellipsometry have been developed by combing imaging techniques with different ellipsometry techniques, such as the null ellipsometry [63,64], the rotating-analyzer ellipsometry [65], the rotating-compensator ellipsometry [66], and also the MME [68,69]. Based on the home-made DRC-MME, we have also developed an IMME by adding an imaging lens after the analyzer to the optical path of MME and replacing the spectrometer with a CMOS camera [23,70].

Figure 7 presents the system layout and prototype of the developed IMME in an oblique mode [23,70]. The light beam from a laser-driven light source (LDLS^{TM} Eq-99XFC, Energetiq Technology, Inc., USA) successively passes through an achromatic lens pair L_1 and a monochromator MO (Omni-λ320i, Zolix Instruments Co., Ltd., China) to choose the illumination wavelength. The monochromatic light then passes through another achromatic lens pair L_2 and is focused on the slit side of a fiber F from B&W Tek. The emitted light beam from the round side of the fiber then passes through a collimating lens L_3. The exiting parallel beam from L_3 goes successively through the PSG, reflected by the sample, the PSA, an achromatic imaging lens, and finally goes into a camera (Zyla 5.5 sCMOS, Andor, UK). The imaging lens has a long focal length and an image magnification of 1:1. Considering the oblique illumination in measurement, the camera was mounted with a slight tilt with respect to the optical axis to obtain a clear image of the entire sample surface. Currently, the spectral range of the instrument is about 400–700 nm, which is mainly limited by the quantum efficiency of the adopted camera and can be easily

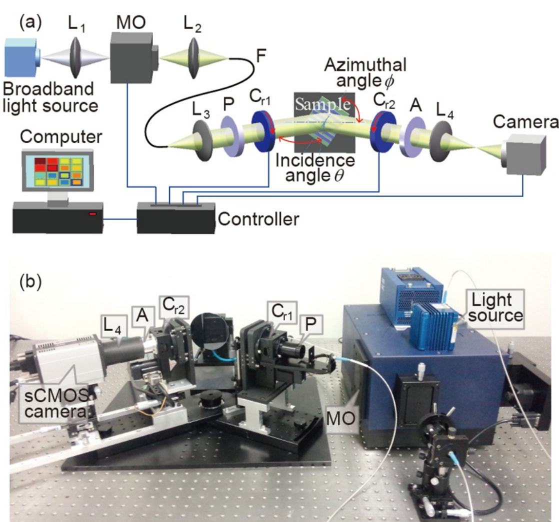

Figure 7 (Color online) (a) System layout and (b) prototype of the developed IMME in an oblique mode, adapted from refs. [23,70]. L_1 and L_2, focusing lens; MO, monochromator; F, fiber; L_3, collimating lens; P and A, polarizer and analyzer; C_{r1} and C_{r2}, the 1st and 2nd rotating-compensators; L_4, imaging lens.

extended to a broader or other band by replacing the camera.

Since the polarization effect of the imaging lens is negligible, the developed IMME in the oblique mode can be calibrated in the same way as the broadband DRC-MME. The 1951 USAF resolution test target as well as a self-designed trench test sample were measured by the developed IMME to examine its lateral resolution. The trench sample was prepared with 8 line grooves of different widths etched in a SiO_2 layer on a Si substrate. The nominal widths of the 8 grooves were 10, 20, 40, 60, 80, 100, 150, and 200 μm, respectively. Figure 8(a) presents the image of the 1951 USAF target collected by IMME at the wavelength of 500 nm. As can be observed, the largest set of distinguishable horizontal and vertical lines corresponds to element 3 of group 5, which indicates that the maximum resolution is about 24.8 μm per line pairs. Figure 8(b) shows the reconstructed map of the grooves. As can be seen, the grooves with widths of 10 and 20 μm cannot be distinguished, while the groove with a width of 40 μm can be visualized with at least on pixel. It indicates that the actual lateral resolution of the instrument is better than 40 μm. Other test results about the measurement accuracy and precision as well as experiments on a series of standard SiO_2/Si films can be found in ref. [23].

Further improvement of the lateral resolution of the above developed IMME may be achieved by replacing the adopted imaging lens L_4 with one with a higher NA. However, in the oblique illumination mode, the improvement is finally limited by the available imaging lens required with both a high NA and a long working distance. To further improve the lateral resolution of IMME, we have developed a vertical mode IMME by adopting a design in which the incident end and the reflection end share a part of the optical path. Figure 9 presents the system layout and prototype of the developed IMME in a vertical mode [24,71]. The light beam from a supercontinuum laser source (WhiteLase SC-400, NKT Photonics, Inc., Denmark) enters a monochromator MO (LLTF, NKT Photonics, Inc., Denmark) and passes through a collimating lens CL. The collimated beam then goes successively through the self-designed anti-speckle module AS, rotatable flat mirror M_r, PSG, non-polarizing beam splitter BS, imaging lens IL, and objective lens OL (EC Epiplan - Apochromat 50 ×/ 0.95 HD DIC, Zeiss, Inc., Germany). After that, the light is reflected by the sample, and successively passes through the OL, IL, BS, PSA, relay lens-pair RL, and finally enters the camera (Zyla 5.5 sCMOS, Andor, UK). As is known, ellipsometry measurement is typically carried out at oblique incidence with incidence angles near the Brewster angle for thin film samples. To change the incidence angles in measurement, we have proposed a back focal plane (BFP) scanning method [24]. As shown in Figure 9(b), the plane of incidence is jointly defined by the PSG and PSA, which is perpendicular to the rotation axis of the flat mirror M_r. The different points on the BFP of the OL correspond to different incidence angles. We can thereby change the rotation angle of the flat mirror M_r to transform the angle of parallel light entering the imaging lens IL. The imaging lens then works as a relay station to focus the parallel incident beam into different points on the BFP of the OL to achieve different incidence angles. Ideally, the maximum incidence angle would be $\sin^{-1}(NA)$, with NA being the numerical aperture of the OL. For the adopted OL in the developed IMME, the actual range of incidence angles is 0°–65°.

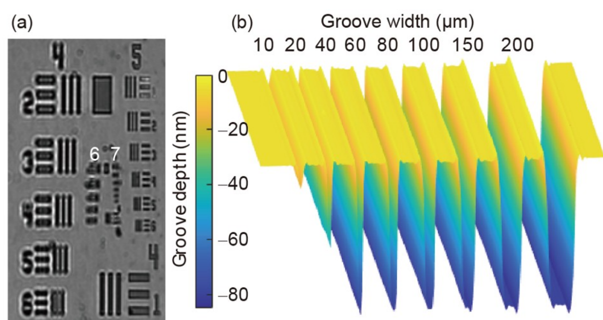

Figure 8 (Color online) Test results for the lateral resolution of the developed IMME in the oblique mode. (a) 1951 USAF target image at 500 nm wavelength; (b) reconstructed map of SiO_2 grooves etched on Si substrate. Adapted from ref. [23].

Figure 10(a) presents the image of the 1951 USAF resolution test target by IMME at the wavelength of 690 nm. According to Figure 10(a), the resolution of the instrument in the working band is better than 0.78 μm. Figure 10(b) shows the resolution results measured by the modulation transfer function test target. It can be seen that when the modulation factor is 5%, the line pair is 1250 lp/mm at 700 nm wavelength, which indicates that the resolution of the instrument reaches 0.8 μm. Figure 10(c) further presents the reconstructed map of self-designed SiO_2 grooves with different widths etched in Si substrate. As can be observed, the grooves with widths of 1 and 3 μm can be clearly distinguished. According to Figure 10, we can conclude that the lateral resolution of the developed IMME in the vertical mode can reach better than 0.8 μm.

Although the developed IMME in the vertical mode achieves a much higher lateral resolution than its counterpart in the oblique mode, the introduction of the high NA OL in the vertical mode also complicates the system calibration. In the vertical mode IMME, besides the system parameters in the PSG and PSA, the high-NA OL and the beamsplitter BS are both required to be calibrated to achieve accurate measurement [72]. Two methods have been proposed for the calibration of the vertical mode IMME, namely, the mode-based method [24] and the model-free method [73].

In the model-based calibration method, all the optical components to be calibrated need to be parameterized first. Here, the amplitude ratio and phase difference (Ψ_{bt}, Δ_{bt}) in the transmission mode and (Ψ_{br}, Δ_{br}) in the reflection mode

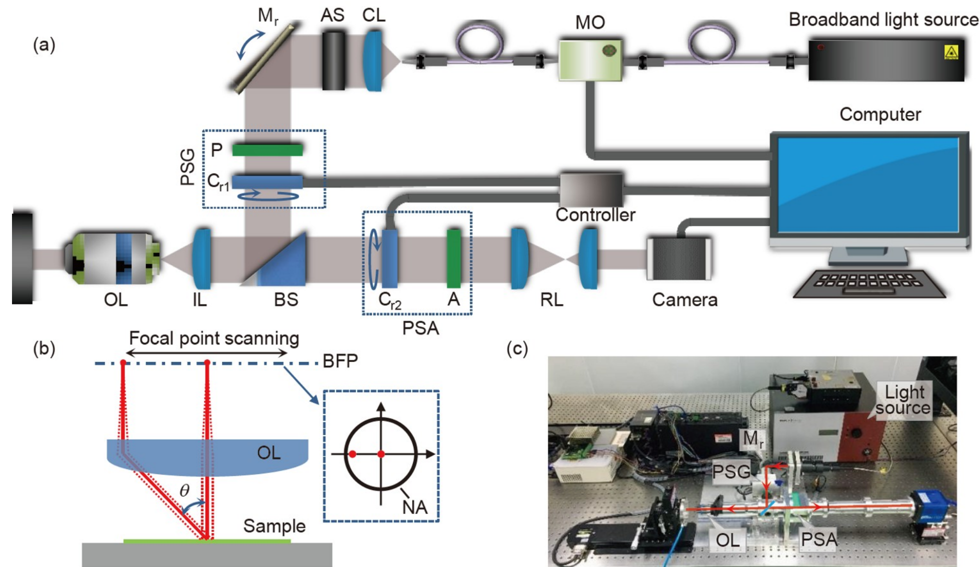

Figure 9 (Color online) (a) System layout and (c) prototype of the developed IMME in a vertical mode; (b) schematic of the back focal plane scanning principle, adapted from ref. [24]. MO, monochromator; CL, collimating lens; AS, anti-speckle module; M_r, rotating flat mirror; P and A, polarizer and analyzer; C_{r1} and C_{r2}, the 1st and 2nd rotating compensators; BS, non-polarizing beamsplitter; IL, imaging lens; OL, objective lens; RL, relay lens-pair.

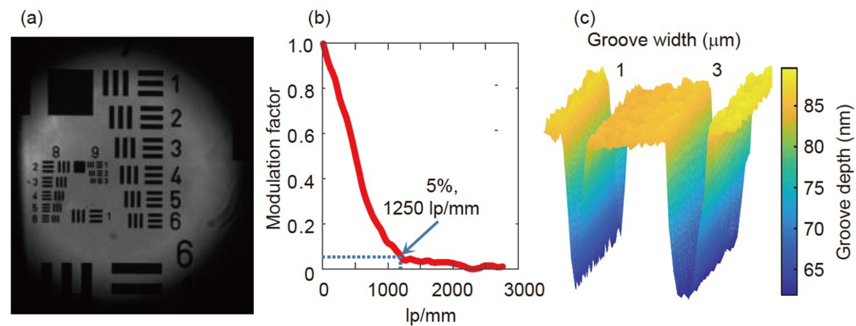

Figure 10 (Color online) Test results of the lateral resolution of the developed IMME in the vertical mode, adapted from ref. [24]. (a) 1951 USAF target image at 690 nm wavelength; (b) modulation factor measured at 700 nm wavelength using the MTF test target; (c) reconstructed map of SiO_2 grooves with the nominal widths of 1 and 3 μm etched on Si substrate.

are used to characterize the polarization effect of the BS. Eight Zernike coefficients are used to characterize the polarization effect of the high-NA OL. By solving the nonlinear least squares optimization problem between the measured and simulated Mueller matrices, the system parameters to be calibrated can be obtained, and the solution process can be optimized by a nonlinear fitting algorithm. The main advantage of the model-based calibration method is that by accurately modeling all optical components to be calibrated, the results obtained are relatively accurate and reliable. However, it also has certain shortcomings, that is, the accuracy of component modeling is very high, and at the same time, when there are some unknown parameters in the system, the calibration results will also be affected.

For model-free calibration method, also named as the extended eigenvalue calibration method (extended ECM), instead of considering the individual effects of each optical component in the instrument, all the factors are combined and calibrated together as a black box. Four samples were used for calibration: air, polarizers at azimuth angles of 0° and 90°, and a waveplate at azimuth angle of 30°. By constructing a semi-positive definite matrix and obtaining the eigenvector whose unique eigenvalue is 0, the matrices associated with the PSG and the PSA can be uniquely determined, and then the calibration of the system is completed. The main advantage of the model-free method is that there is no need to know the specific components in the system. When there are many free components and error sources in the measurement system, the model-free method can enable simpler calibration of the full Mueller matrix measurement system compared with the model-based calibration method. However, it should be noted that the model-free calibration process relies on the measurement of 4 different samples, which may have the problem of amplifying the sources of error and increase the risk of calibration, and the robustness is not as good as that of the model-based method.

3.3 High-speed Mueller matrix ellipsometer

Compared with the above MME, the high-speed Mueller matrix measurement has the advantage of being able to quickly measure the Mueller matrix of a sample with the measurement time much less than second-scale. We have developed a high-speed MME (HSMME) [25], in which the principle of dual-PEMs polarization modulation as the PSG and the DoA polarization demodulation as the PSA has been utilized [74,75]. Figure 11(a) depicts the basic system optical layout of the developed HSMME, where the PSG module consists of a polarizer and dual-PEMs and the PSA module consists of six channels of polarization analyzers. Since both the two PEMs can be considered as dynamic phase retarders with the tuning frequency of the phase retardation larger than 47 kHz [42], the Stokes vector $\mathbf{S}_{\mathrm{PSG}}$ of incident light emerged from the PSG can be fast changed in temporal as

$$\begin{aligned}\mathbf{S}_{\mathrm{PSG}}(t) &= \left[S_0(t)\ \ S_1(t)\ \ S_2(t)\ \ S_3(t)\right]^{\mathrm{T}} \\ &= \mathbf{M}_{\mathrm{C}}(\delta_{\mathrm{PEM2}}(t),\phi_{\mathrm{PEM2}})\mathbf{M}_{\mathrm{C}}(\delta_{\mathrm{PEM1}}(t),\phi_{\mathrm{PEM1}})\mathbf{M}_{\mathrm{P}}(-\phi_{\mathrm{P}})\mathbf{S}_{\mathrm{in}},\end{aligned} \quad (19)$$

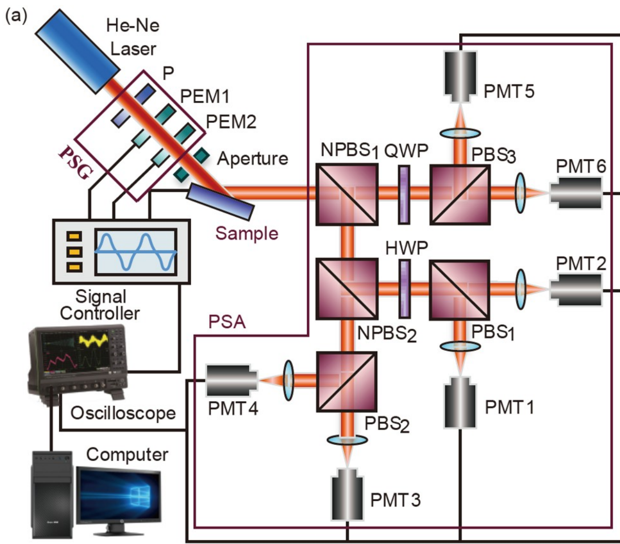

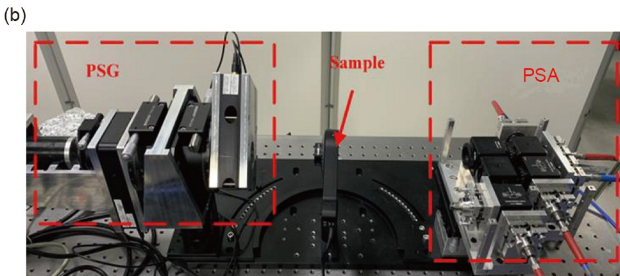

Figure 11 (Color online) (a) System layout and (b) prototype of the developed high-speed MME, adapted from ref. [25]. PEM, photoelastic modulator; NPBS, non-polarizing beamsplitter; PBS, polarizing beamsplitter; QWP, quarter-wave plate; HWP, half-wave plate; PMT, photomultiplier tube.

where ϕ_{PEM1} and ϕ_{PEM2} are orientation angles of fast axes of PEM1 and PEM2, respectively, $\delta_{\mathrm{PEM1}} = \delta_{\mathrm{p1}}\cdot\sin(2\pi f_1 t + \varphi_1) + \delta_{\mathrm{s1}}$ and $\delta_{\mathrm{PEM2}} = \delta_{\mathrm{p2}}\cdot\sin(2\pi f_2 t + \varphi_2) + \delta_{\mathrm{s2}}$ are the temporal phase retardances of PEM1 and PEM2, respectively. Both the peak phase retardances δ_{p1} and δ_{p2} are dependent on the actual driving voltage of the PEM, while the static retardances δ_{s1} and δ_{s2} are dominated by the crystalline properties of the photoelastic crystal in the PEM, f_1 and f_2 are the nominal frequencies of PEM1 and PEM2, respectively, and t is the time.

Through introducing a light intensity matrix $\mathbf{B}$ to express the intensity data reported by the six photomultiplier tubes (PMT) in the six demodulating channels [76], the system model of the HSMME can be described as follows:

$$\begin{aligned}\mathbf{B}(t) &= \left[i_1(t)\ \ i_2(t)\ \ i_3(t)\ \ i_4(t)\ \ i_5(t)\ \ i_6(t)\right]^{\mathrm{T}} \\ &= \mathbf{A}_{\mathrm{PSA}}\mathbf{M}_{\mathrm{S}}\mathbf{S}_{\mathrm{PSG}}(t) \\ &= \left[\mathbf{a}_1\ \ \mathbf{a}_2\ \ \mathbf{a}_3\ \ \mathbf{a}_4\ \ a_5\ \ \mathbf{a}_6\right]^{\mathrm{T}}\mathbf{M}_{\mathrm{S}}\mathbf{S}_{\mathrm{PSG}}(t),\end{aligned} \quad (20)$$

where the demodulating matrix $\mathbf{A}_{\mathrm{PSA}}$ is composed of the first row vector $\mathbf{a}_j$ (j = 1–6) of the matrix obtained by multiplying the Mueller matrix of each optical component in the six channels, and the detailed form of $\mathbf{a}_j$ is given in ref. [77].

After using the Levenberg-Marquardt algorithm to fit the measured intensity set $\mathbf{B}_{\mathrm{m}}$ with the calculated intensity set $\mathbf{B}_{\mathrm{c}}$ reported by the system model, both the sample Mueller matrix $\mathbf{M}_{\mathrm{s}}$ and the initial phases $\boldsymbol{\varphi} = \{\varphi_1,\varphi_2\}$ can be extracted at the same time [25], as described as follows:

$$\begin{aligned}[\mathbf{M}_S,\ \boldsymbol{\varphi}] = \underset{M_S\in\Omega,\ \varphi\in\Gamma}{\operatorname{argmin}} &\left[\mathbf{B}_m - \mathbf{B}_c(\mathbf{p},\ \mathbf{M}_S,\ \boldsymbol{\varphi})\right]^{\mathrm{T}} \\ &\cdot \Sigma_{\mathbf{B}_m}^{+}\left[\mathbf{B}_m - \mathbf{B}_c(\mathbf{p},\ \mathbf{M}_S,\ \boldsymbol{\varphi})\right],\end{aligned} \quad (21)$$

where $\mathbf{p}$ is the system parameters set which is determined by the pre-calibration of the instrument, and $\Sigma_{\mathbf{B}_m}^{+}$ is the Moore-Penrose pseudo-inverse of the covariance matrix $\Sigma_{\mathbf{B}_m}$ of the measured intensity matrix [25].

In order to ensure the measurement of Mueller matrix $\mathbf{M}_{\mathrm{s}}$ with high temporal resolution, the mutually uncorrelated Stokes vectors produced by the PSG should be much more than 16 and should be suffering at least one cyclic change in a single extreme-short-time measurement. Meanwhile, for ensuring both the same high accuracy and the strong robustness of $\mathbf{M}_{\mathrm{s}}$ in each measurement cycle, the *in-situ* calibration of some critical components in the system such as PEMs and beamsplitters is essential. Correspondingly, we have proposed a novel approach based on both the fast Fourier transform and the Bessel function expansion to ensure the precise *in-situ* parameters calibration of PEM [25]. At the same time, a method based on the polar decomposing of Mueller matrix has been proposed to calibrate all the feature parameters of the beamsplitter, such as depolariza-

tion, linear and circular birefringence, as well as linear and circular dichroism [77]. With the proposed method, the general error of the Stokes vector measured by the PSA in the HSMME can be reduced from 3% to less than 1%. Besides, considering the achievable phase retardation of 0 to 6π realized by PEM, we have introduced a period-division method to improve the measurement temporal resolution of the Mueller matrix [25], that is,

$$T=\frac{2\pi}{\left|f_1\delta_{p1}-f_2\delta_{p2}\right|}. \tag{22}$$

It should be noted that the above period-division method would work best when the peak retardation angles of the PEMs are tuned as the integer multiple of 2π. Specifically, through setting the peak retardation angles of the PEMs as 6π and 2π respectively, the temporal resolution of the HSMME can be increased from about 11 to 300 μs.

Figure 11(b) presents the prototype of our developed HSMME. The light source is a 5 mW CW He-Ne Laser (HNL050LB, Thorlabs, USA) with central wavelength of 632.8 nm, and the polarizer (LPVIS100-MP2, Thorlabs, USA) is a nanoparticle linear film polarizer with an extinction ratio up to 100000:1. The nominal frequency of the PEM1 and PEM2 (II/FS47, II/FS50LR, Hinds, USA) are 47.112 and 50.006 kHz, respectively. Through adopting the above components configuration, the PSG can generate a polarized light beam with any polarization state. It is worth emphasizing that by setting the driving voltages of PEM1 and PEM2 as 4.80 and 1.56 V, respectively, the phase retardation angles of PEM1 and PEM2 can be 6π and 2π, respectively. The PSA module is composed of two NPBSs (Non-polarizing BS019 and BS013, Thorlabs, USA) with split ratios of 7:3 (R:T) and 5:5 (R:T), respectively, a quart-wave plate (WPMQ05M-633, Thorlabs, USA), a half-wave plate (WPMH05M-633, Thorlabs, USA), three PBSs (CCM1-PBS25-633/M, Thorlabs, USA), six photomultiplier tubes (PMT, H10721 Series, Hamamatsu, Japan) and an oscilloscope (WaveSurfer-3000, Teledyne Lecroy, USA). The above-mentioned DoA demodulation configuration, the 0.57 ns response time of the PMTs and the 200 MHz signal acquisition rate of the oscilloscope enable the PSA module to detect the Stokes vector of the reflected or transmitted light with a temporal resolution less than several nanoseconds. Finally, the compromise between the modulation efficiency of the PSG and the demodulation efficiency of the PSA allows the instrument to achieve a temporal resolution of 11 μs for the Mueller matrix measurement.

In order to demonstrate the high temporal resolution of HSMME, the process of a quarter-wave plate (QWP) modulating the Stokes vector $\mathbf{S}_{\mathrm{PSG}}$ produced by the dual-PEMs has been characterized by the self-developed HSMME. The corresponding measurement results are presented in Figure 12. As can be observed, the period of the Stokes vector $\mathbf{S}_{\mathrm{PSG}}$ is 10.95 μs, which indicates that the temporal resolution of Mueller matrix measurement is better than 11 μs. Figure 13 presents the measured and fitted mean Mueller matrices of the QWP under different azimuth angles after successive 15 measurements, in which the measured and the fitted results are highly consistent. Moreover, all the standard deviations of each Mueller matrix element are less than 0.003. These results also demonstrate the high accuracy and repetitive precision.

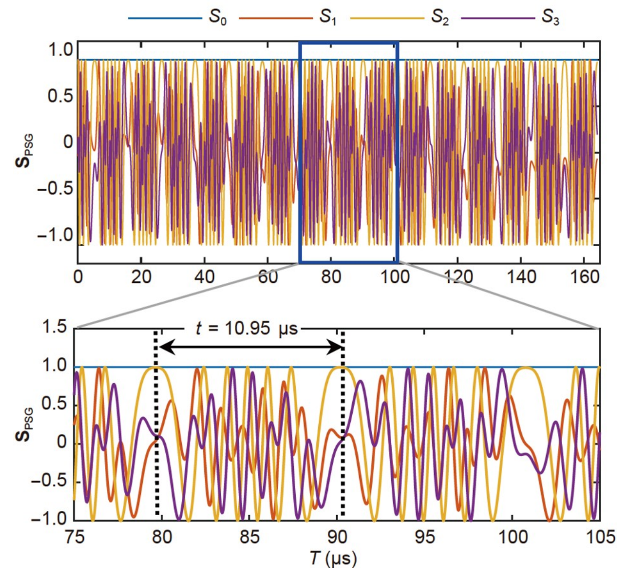

Figure 12 (Color online) The measured time-variant Stokes vector $\mathbf{S}_{\mathrm{PSG}}$ before the modulation of a QWP. Adapted from ref. [25].

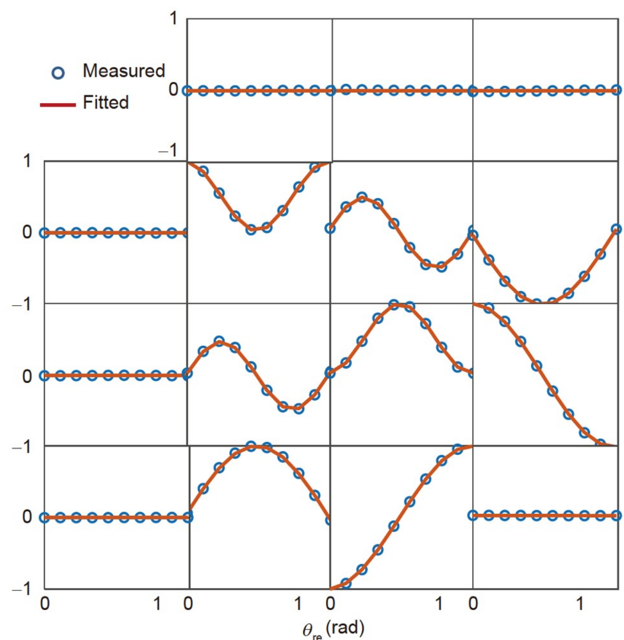

Figure 13 (Color online) Measured and fitted mean Mueller matrices of a QWP under different azimuth angles after 15 repeated measurements. Adapted from ref. [25].

4 Emerging applications

4.1 Two-dimensional materials characterization

Optical constants, including the complex refractive index, the complex dielectric constant, and the optical conductivity, are basic optical and physical data for optoelectronic materials, which reflect the light-matter interactions, such as the light propagation and dissipation in the media. Accurate determination of the optical constants is of basic science for fields of materials and physics, which can not only help us to understand novel optoelectronic phenomena and reveal the behind physical mechanisms, but also guide the optimal design of related optoelectronic devices. The SE deals with polarized light-matter interactions. Since an additional dimension of light, namely the polarization, is introduced, the SE can gain much more information about the samples than conventional optical metrology techniques, which makes it a powerful and standard tool to characterize the optical constants and thicknesses of nanofilms and nanomaterials. Low dimensional materials, such as 2D materials, quasi-1D crystals, photonic crystals, metamaterials, etc., are the most promising materials for the next-generation microelectronics and optoelectronics due to their unique and outstanding photoelectric properties, such as high carrier mobility, optical anisotropy, tunability, flexibility, integration, etc. With the help of the developed advanced ellipsometers, we have established a database of basic optical constants for a series of emerging 2D materials and quasi-1D crystals, and studied their optical and dielectric properties during the past years.

Due to the strong correlation between optical constants and film thicknesses in the ellipsometry analysis of ultra-thin films [8], the accurate characterization of ultra-thin films by SE has always been a challenging issue. To deal with the characterization of ultra-thin films, a completely analytical method based on the 2nd-order Taylor expansion of Drude's ellipsometric functions is proposed to determine the complex refractive index of ultra-thin materials, as illustrated in Figure 14 [78]. In this method, we should know the complex refractive indices of the surrounding (i.e., air) and the substrate beforehand, which can be easily determined by SE. Then we can directly obtain the complex refractive index of the thin film from the measured ellipsometric angles with the incidence angle and film thickness. Results have indicated that the proposed method can be applied to deal well with the ellipsometry analysis of ultra-thin films with thickness less than 5 nm over an ultra-wide spectral range covering UV-VIS-IR without prior knowledge about electronic transitions of the material. The complex dielectric constants can be directly converted from the complex refractive index. Also, the complex optical conductivity of an ultra-thin film can be calculated from its complex refractive index and the measured ellipsometric spectra by using the classical slab model and the surface current model. With this method, we have determined the optical constants of several typical ultra-thin 2D materials, including the graphene, 2D transition metal chalcogenides (TMDCs), etc.

Based on the optical constants, we have systematically investigated the layer-dependent optical and dielectric properties of typical 2D materials, including the graphene [79,80], 2D TMDCs (e.g., MoS_2, WSe_2, $Mo_{1-x}Nb_xS_2$, etc.) [81–85], 2D Bi_2Se_3 [86,87], 2D hybrid perovskites [88], etc. Figure 15 shows the complex dielectric constants of 2D MoS_2 with thickness ranging from a monolayer to the bulk, as well as the layer-dependent evolutions in the magnitudes and central energies of feature peaks [81]. It can be seen that due to the synthetic influences of the excitonic effect, the joint density of states and the mass density, the center energies of these feature peaks exhibit intriguing layer dependency, and the imaginary part of the complex dielectric constant exhibits a "W" like curve versus the thickness with two valley bottoms appearing at about 4-layer and 10-layer, respectively. By using the critical point (CP) analysis [8,11], we can further obtain information about the optical transitions at these CPs, including the energies, the shape, and the type. Combining with the first-principle calculations, positions of these optical transitions in band structure, as well as the bands and carriers involved in the transitions can be identified. Figure 16 shows the results about the identification of optical transitions of the monolayer WSe_2 by combining the SE, the CP analysis, and the first-principle calculations [83]. Based on these methods and results, we have additionally revealed influences of the excitonic effect,

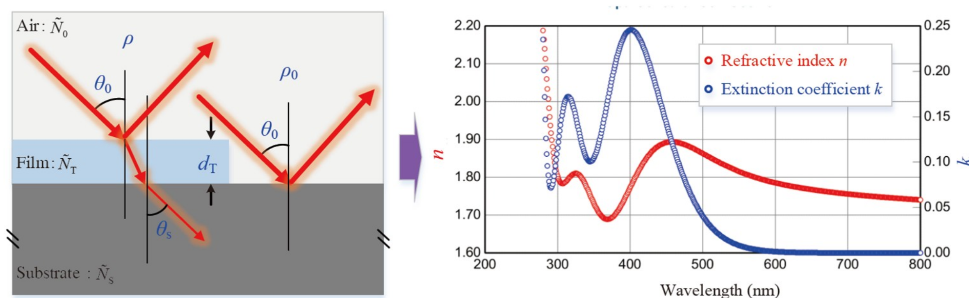

Figure 14 Principle of the analytical ellipsometry for ultra-thin films based on the 2nd-order Taylor expansion of Drude's functions. Adapted from ref. [78].

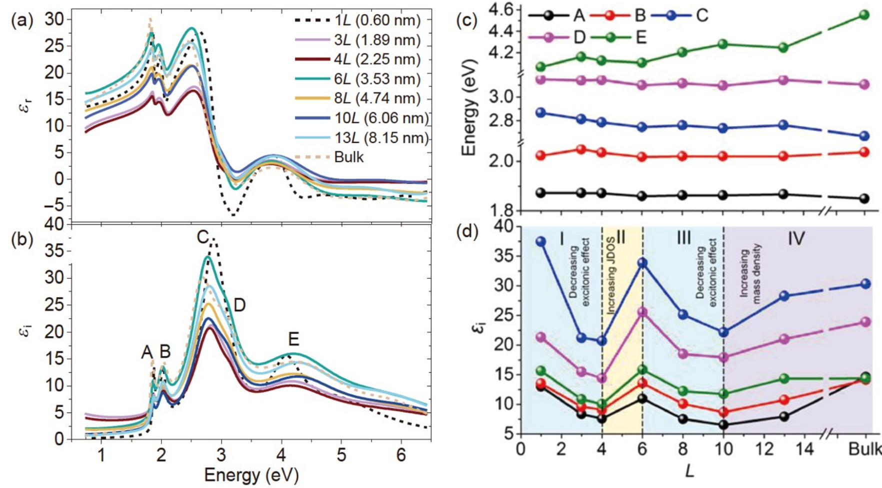

Figure 15 Layer-dependent dielectric properties of 2D MoS_2. (a) The real part and (b) the imaginary part of the dielectric constants of MoS_2 with thicknesses varied from a monolayer to the bulk; (c) evolutions of the central energies of the feature peaks in the dielectric functions versus the layer number L; (d) evolutions of the imaginary part of the dielectric constants at the feature peaks versus the layer number L. Adapted from ref. [81].

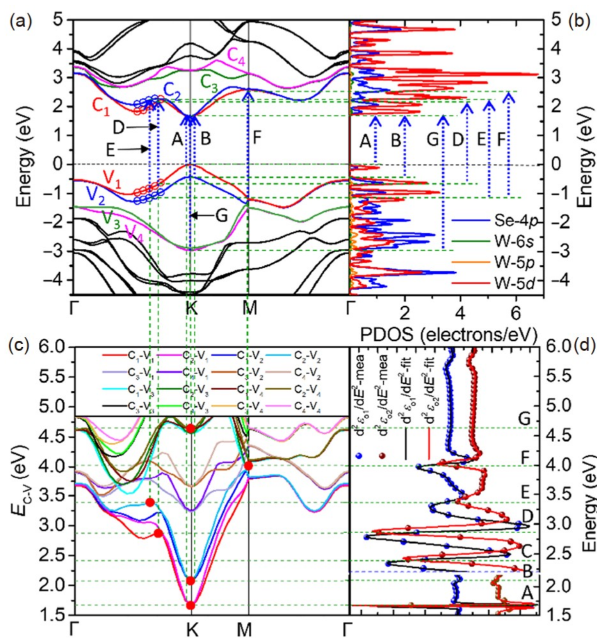

Figure 16 Identification of optical transitions of the monolayer WSe_2. (a), (b) First-principle calculated band structure and projected density of states; (c) energy differences between the first four conduction bands and the first four valence bands; (d) CP analysis results. Adapted from ref. [83].

band shrinkage, surface state hybridization, thickness scaling effect, and the layer stacking order on the evolutions of the optical and dielectric properties of 2D materials [79–88].

Low-dimensional materials will always exhibit remarkable optical anisotropy due to the asymmetries in lattice structures or dimensional scales, which make them promising candidates for polarization-sensitive applications [79,83,89–92]. Taking advantage of the abundant information provided by the MME, we have studied the optical anisotropy of several typical low-dimensional materials, including the quasi-1D $ZrTe_5$ [89], quasi-1D transition metal trichalcogenides (e.g., TiS_3, ZrS_3) [90], and 2D SnSe [91], etc. Figure 17 shows the low lattice structures and the optical anisotropy of quasi-1D $ZrTe_5$ crystal [89]. With the broadband MME, the complete dielectric tensor was firstly determined as shown in Figure 17(c) and (d). Then the in-plane optical anisotropy was quantitatively evaluated by calculating the birefringence and dichroism as shown in Figure 17(e) and (f). It can be seen that the $ZrTe_5$ crystal demonstrates giant dispersive birefringence and dichroism, e.g., the birefringence Δn reaches 0.58 at the wavelength of 942 nm. By combining the CP analysis and first-principle calculations, the specific interband transitions related to the CPs in dielectric function spectra along three crystal axes of $ZrTe_5$ are identified, revealing the physical essence of the optical anisotropy from a perspective of quantum mechanics.

Due to the lack of large-area growth processes, many novel 2D materials are prepared by mechanical exfoliation, which cannot be characterized using traditional SE. It is because the lateral resolution of traditional SE is determined by the illumination spot, which is typically much larger than the size of the exfoliated 2D materials. To characterize the optical properties of these novel 2D materials, the imaging ellipsometry with a higher lateral resolution should be used. Figure 18(a) presents the optical micrograph of a 2D GeS_2 flake with a size of about 1.5 μm × 2.5 μm on a glass substrate, which is a typically in-plane anisotropic layered material with excellent optical and electrical properties [24]. We employed the developed IMME to characterize the anisotropic optical properties of GeS_2. The sample was measured by IMME at the spectral range 410–700 nm, the incidence angle of 60°, and the azimuthal angles of 0°, 30°, and 60°. Using the data collected at multi-azimuths, the information

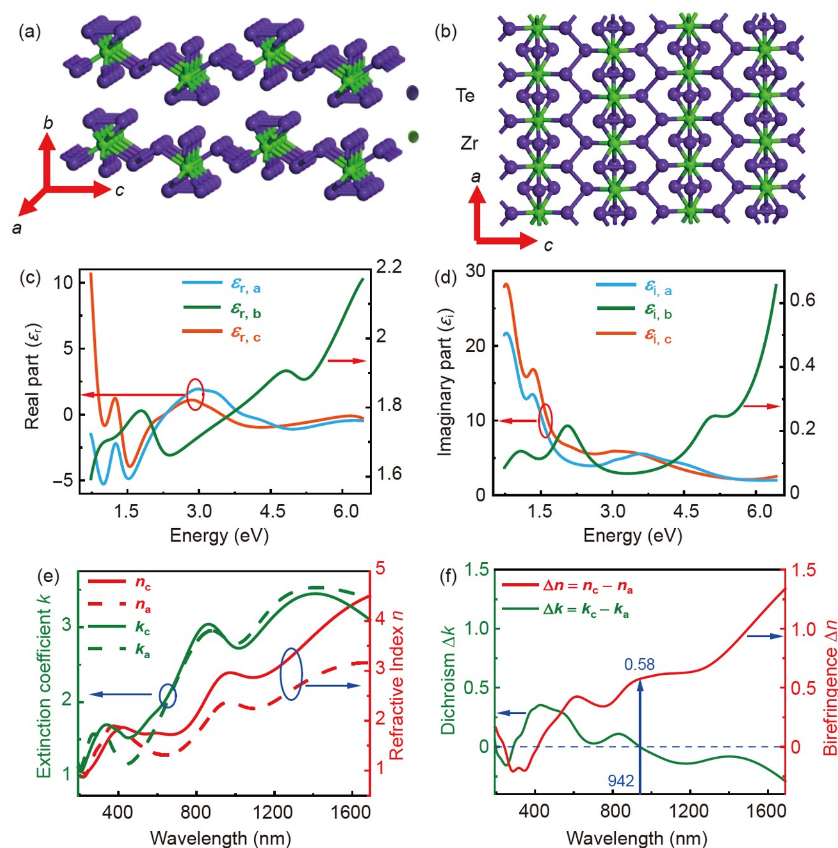

Figure 17 (a) Side view and (b) top view of the lattice structure of $ZrTe_5$; (c) the real part and (d) imaginary part of the dielectric tensor of $ZrTe_5$; (e) in-plane refractive indices and extinction coefficients; (f) in-plane birefringence and dichroism. Adapted from ref. [89].

of anisotropic samples can be fitted more accurately. The ellipsometry data analysis was performed for a selected pixel of the IMME camera near the center of the GeS_2 region. In the analysis, the dielectric function of GeS_2 was modeled with the Tauc-Lorentz oscillators. Figure 18(b) shows the fit result between the measured and calculated best-fit Mueller matrix spectra. Figure 18(c) gives the analyzed optical constants of GeS_2 in the x, y and z directions. The fit thickness of the GeS_2 film was (18.6±1.33) nm (95% confidence level). The corresponding thickness measured by AFM, as shown in Figure 18(a), was (17.5±0.78) nm, which was in good agreement with the IMME result.

4.2 Organic materials characterization

Organic materials, especially organic semiconductors are widely applied in optoelectronics devices, such as the OPV and OLED, which have been of the hot research topics during the past decades. Optical properties of organic materials and layer thicknesses have significant influences on the key performances, including the efficiency and the chromaticity of related stratified devices [93–96]. Therefore, accurate characterization of the optical constants and film thicknesses of organic layers is essentially important for the optical analysis and optimal design of the organic devices.

With the developed broadband MME, we have accurately characterized the thicknesses of nanofilms in the multilayer stack structure, as well as the complex refractive indices and dielectric functions of the organic materials of OLED/OPV devices. Figure 19 shows the schematic diagram of a tandem organic solar cell (OSC) and the complex refractive indices and film thicknesses of the materials involved in the device characterized by MME [97]. A basic database of optical functions is constructed for typical organic semiconductors for the OLED and OPV. Additionally, optical properties of organic materials, such as the molecular orientation and optical anisotropy, can be further investigated [96].

In order to analyze and optimize the optical performances of stratified optoelectronics devices, optical simulation models were constructed for both the active multilayer structure and the passive multilayer structure based on the computational electromagnetics methods [97–100]. In the optical modelling, complex features, such as the optical anisotropy, nanostructures, coherent-incoherent hybridization, etc., were considered [98,99]. Figure 20 shows the schematic of a coherent-incoherent hybrid OSC with periodic nanostructures and its optical modelling, in which the bidirectional scattering distribution functions (BSDF) was applied to deal with the nanostructures and a correction factor was introduced to consider the incoherent glass substrate [98].

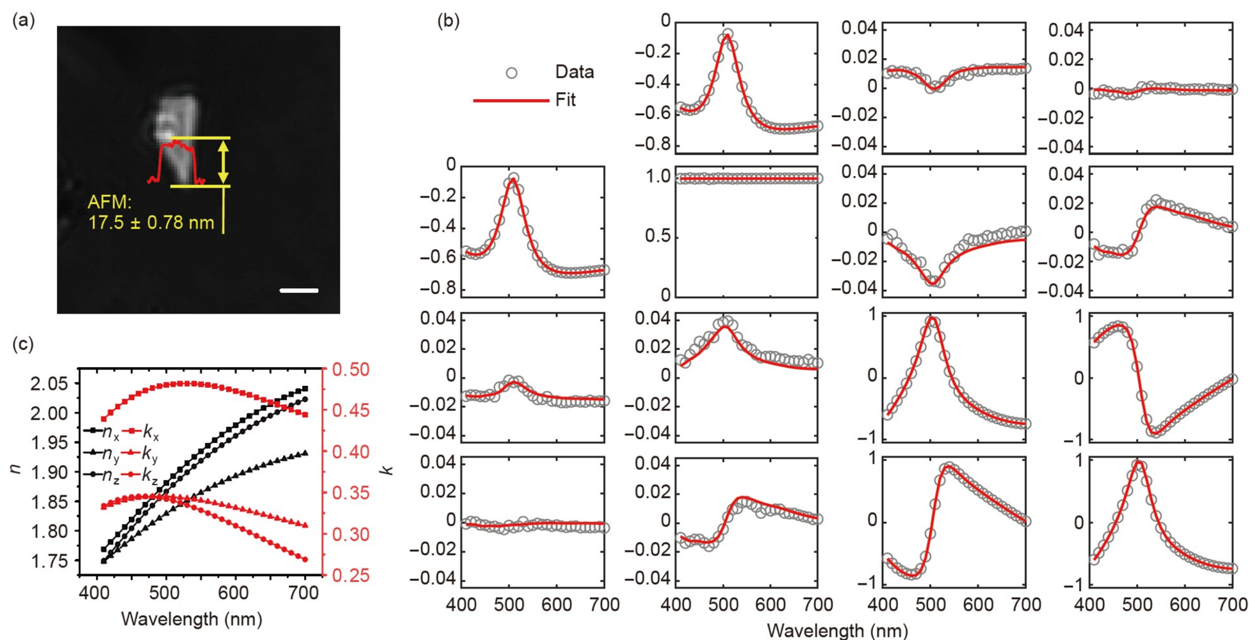

Figure 18 (a) Optical micrograph of the 2D GeS_2 on glass substrate overlaid with the AFM measured result (the scale bar is 1 μm); (b) fit result of the measured and calculated best-fit Mueller matrix spectra at the incidence angle of 60° and azimuthal angle of 30°; (c) the obtained optical constants of GeS_2. Adapted from ref. [24].

Based on the information obtained by MME and the constructed models, high-throughput simulations can be performed to analyze the optical performances of the OLED and OPV devices [93,99]. Figure 21 shows the structure layout of a prototypic OLED device and its optical modelling, as well as the simulation results about the outcoupling efficiency as a function of the ETL thickness under different radiative quantum efficiency for vertical dipoles (VED) and horizontal dipoles (HED) [99]. Further, these information and analysis can provide strong guidance for the optimal design of OLED and OPV devices to synergistically improve key performances [97,98,100], such as the efficiency, the chromaticity, and the angular dependency, etc. Figure 19(c) and (d) present the optimized results of the tandem OSC considering the incidence change during a whole day compared with results of a conventional device designed only for the normal incidence [97]. It can be seen that the optimized tandem device has a more balanced current match at all incident angles during a whole day. Experimental results have demonstrated that the generated energy density per day of the optimized tandem device has notably increased compared with the conventional device optimized only at the normal incidence.

4.3 Dynamic optical properties characterization

Transient responses of materials under external physics field loading such as high temperature, magnetic excitation and voltage driving are of great importance in the study of manufacturing processing and micro/nano sensors development [101]. Since the duration of the mentioned dynamic loading and corresponding response is extremely short, typically less than 10 ms, accessing the transient optical properties of materials by the RAMMP with high temporal resolution enables us to deeply understand the underlying physical mechanisms of these phenomenon. Considering that the nematic LCVRs have been widely used as electrically tunable phase retarder in various RAMMPs [102], dynamic characterization of typical LCVR modulation process is of great importance for the development of RAMMPs.

Relying on the high temporal resolution and the high accuracy of the HSMME, we have reliably characterized the dynamic modulation process of the LCVR (D5220, Meadowlark Optics, USA) under a sawtooth driving signal with a modulation frequency of 50 Hz [25]. Figure 22(a) shows the phase modulation principles of a typical nematic LCVR, in which the orientation of the liquid crystal molecules inside the LCVR changes regularly from with the applied electric field. When there is no external electric field, the liquid crystal molecules between the ITO layers exhibit a natural twist orientation [103]. Meanwhile, the long axis of the liquid crystal molecules is parallel to the surface of the fuse silica window, and correspondingly the LCVR has the maximum phase retardation. With the increase of the applied electric field, the liquid crystal molecules are gradually tilted, which will result in a gradual decrease in the phase retardation of the LCVR. When the applied electric field reaches the maximum, the long axis of the liquid crystal

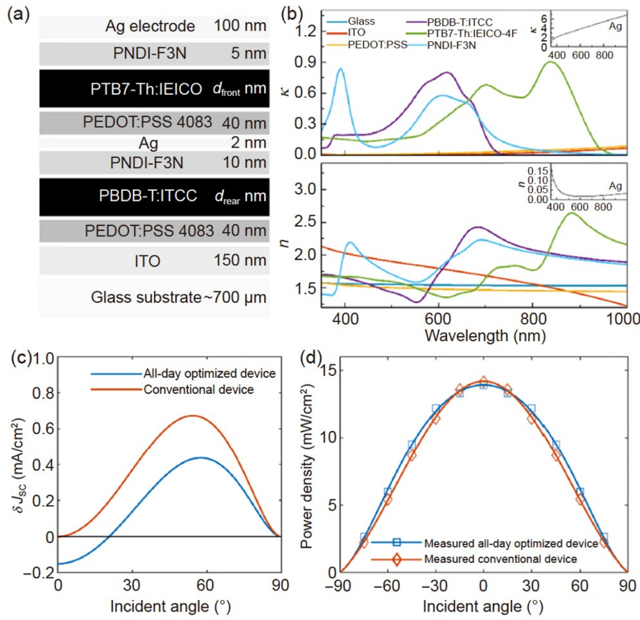

Figure 19 (a) Schematic diagram of the device structure of a tandem OSC given with the material names and thicknesses of the layers; (b) refractive index n and extinction coefficient k of materials employed in the tandem OSC; (c) short current mismatch and (d) measured power density during daytime of the optimized device compared with those of a conventional device. Adapted from ref. [97].

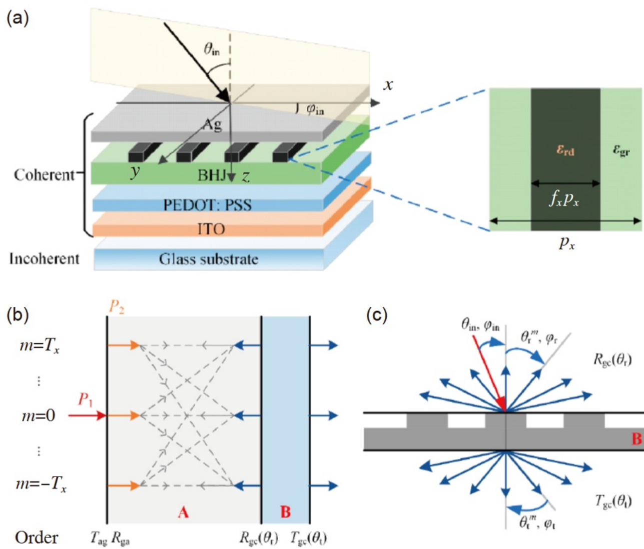

Figure 20 (a) Schematic diagram of the stratified structure of the OSC with one-dimensional metal nanogratings; (b) optical model of the OSC with nanostructured layer based on BSDF, where regions A and B are the incoherent glass substrate and the coherent multilayers containing the nanostructured layers, respectively; (c) schematic diagram of the BSDF model for region B with nanostructured layers. Adapted from ref. [98].

molecules is perpendicular to the surface of the fused silica window, and correspondingly the retardation of the LCVR decreases to the minimum value [103]. Figure 22(b) [103–106] shows the Mueller matrices of LCVR under different voltages, which indicates obvious voltage dependence of the

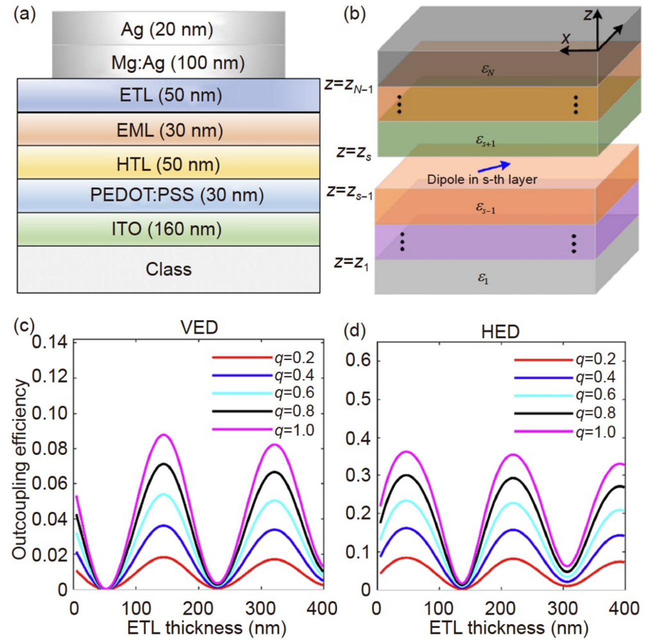

Figure 21 (a) Structure layout and (b) schematic diagram of optical modelling of a prototypic OLED device; (c) and (d) outcoupling efficiency of the OLED stack as a function of the ETL thickness under various radiative quantum efficiency q for VED and HED, respectively. Adapted from ref. [99].

static modulation characteristics. Compared with the previous theoretical models that only consider the linear birefringence (LB), our proposed model considers the LB, the linear diattenuation (LD) and the circular birefringence (CB) simultaneously, so that our proposed model can better match the experimental results.

Figure 23 presents the dynamic LB, LD and CB parameters of LCVR, which were determined by fitting the measured Mueller matrix by HSMME with the calculated Mueller matrix [25]. It can be found that both the optical rotation angle γ_{LC} and the azimuth angle θ_{LC} change drastically with the driving voltage increasing from 1.5 to 4.5 V, which indicates the existence of CB effect in the dynamic phase modulation process of LCVR. Also, the dependency of the relative transmittance A_{LC} and the retardance δ_{LC} on the driving voltage has verified that the dynamic phase modulation characteristics of LCVR vary with the modulation time (i.e., the modulation frequency). The above results could help us predict the Mueller matrices of LCVR at different time points.

4.4 Nanostructure metrology

Process control in microelectronic manufacturing requires real-time monitoring techniques. Due to the inherent non-contact, non-destructive, time-effective, and easy-to-integrated merits, ellipsometric scatterometry has become one of the most important techniques for critical dimension

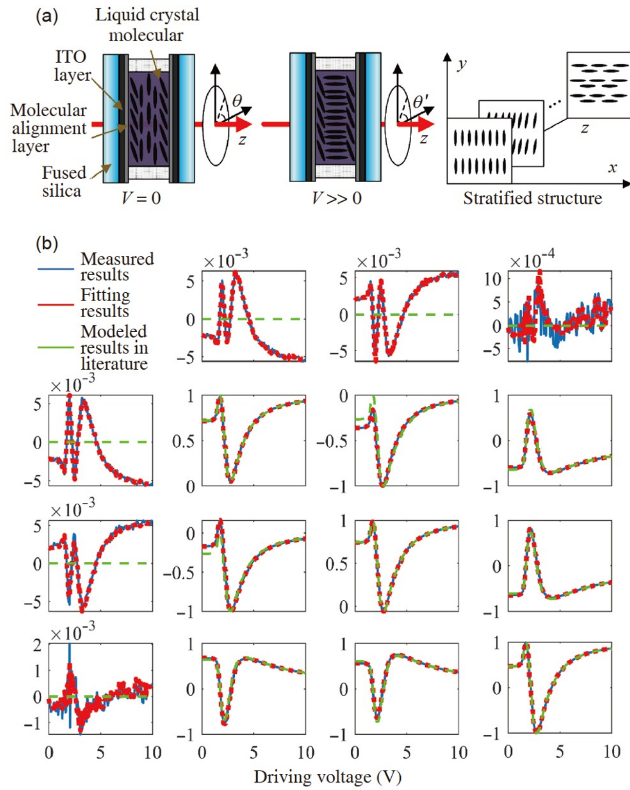

Figure 22 (a) Structure and phase modulation schematic diagram of a nematic LCVR and (b) mueller matrices of LCVR at different voltages (the literature model is cited from refs. [103–106]).

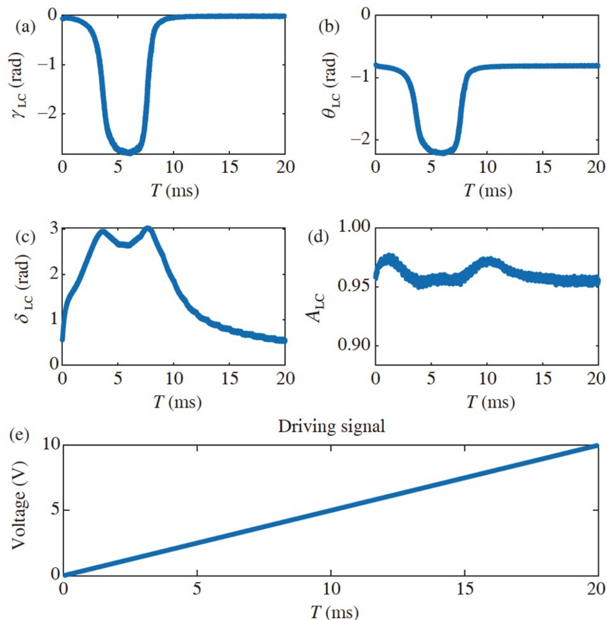

Figure 23 Dynamic optical parameters of LCVR measured by the HSMME. (a) The optical rotation angle γ_{LC} over time; (b) the azimuth angle θ_{LC} over time; (c) the retardance δ_{LC} over time; (d) the relative transmittance A_{LC} over time; (e) the driving signal over time. Adapted from ref. [25].

metrology in semiconductor manufacturing. In comparison with conventional ellipsometric scatterometry, which typically obtains two ellipsometric parameters (Ψ and Δ) at most, the MME-based scatterometry can provide more information about the sample, such as anisotropy and depolarization. By making full use of the information in the collected Mueller matrix spectra, MME-based scatterometry is expected to achieve more precise nanostructure metrology.

Figure 24(a) presents the SEM micrograph of a nanoimprinted resist pattern, which was imprinted using a Si imprinting mold. The Si imprinting mold has gratings with a pitch of 800 nm, a top line width of 350 nm, a line height of 472 nm, and a sidewall angle of 88° [107]. We adopted a symmetrical trapezoidal model with a total of five structural parameters x_1–x_5 to characterize the grating line profile, where x_1, x_2, x_3, x_4 and x_5 represent top critical dimension, line height, sidewall angle, residual layer thickness, and radius of the bottom round corner, respectively. In the fitting procedure, we fixed the grating pitch at 800 nm and just let the parameters x_1–x_5 vary. The optical constants of the STU220 resist were pre-determined from a STU220 resist film deposited on the Si substrate and also fixed in the fitting procedure [108].

In MME-based scatterometry, as illustrated in Figure 4(a), besides the incidence angle θ, the azimuthal angle ϕ can also be adjusted. It has been demonstrated that the change of measurement configurations from the traditional planar diffraction, i.e., with grating lines perpendicular to the incidence plane (ϕ = 0°), to the general conical diffraction ($\phi \neq$ 0°) could help decouple come critical parameters [109]. The measurement configuration optimization [110–112] performed for the investigated nanoimprinted resist pattern revealed that more accurate measurement could be achieved at θ = 65° and ϕ = 15° [108]. The calculation of the depolarization indices (DI) from the collected Mueller matrix spectra showed that the depolarization indices were close to 1 over most of the spectrum except for the range from –380 to 460 nm and showed, as can be observed from Figure 24(c), striking dips to –0.84 near 320 nm. Since DI < 1 indicates depolarization [107], the investigated nanoimprinted grating structure exhibits noticeable depolarization effects that should be considered in the interpretation of the Mueller matrix spectra. It was found the depolarization effects were induced by the finite NA of the focusing lens, the finite spectral bandwidth of the spectrometer, as well as the residual layer thickness variation of the sample [107]. More importantly, it was demonstrated that, by incorporating the depolarization effects into the interpretation of the measured spectra, not only further improvement in the measurement accuracy was achieved, but also the residual layer thickness variation over the illumination spot could be directly determined (σ_t in Table 2) [107,108]. Table 2 presents the comparison of fit parameters obtained from MME and SEM measurements. Good agreement can be observed from this table.

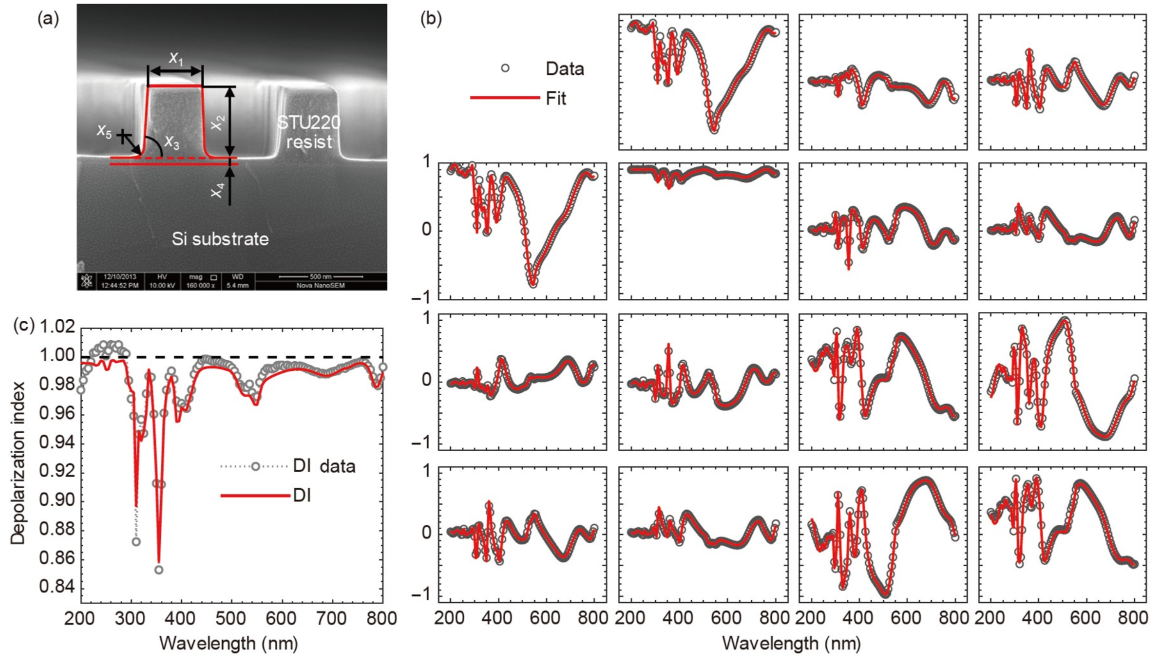

Figure 24 (Color online) (a) SEM micrograph of the investigated nanoimprinted resist pattern overlaid with the adopted geometric model in ellipsometry data analysis; (b) fit result and (c) depolarization index (DI) spectra of the measured and calculated best-fit Mueller matrix spectra when considering the depolarization effects induced by the finite spectral bandwidth and NA of the instrument as well as the residual layer thickness nonuniformity of the sample. Data analysis was performed at $\theta = 65°$ and $\phi = 15°$. The spectral range was varied from 200 to 800 nm with an increment of 5 nm. Adapted from ref. [108].

Table 2 Comparison of fit parameters obtained from MME and SEM measurements. The appended parameter uncertainties correspond to a 95% confidence level, adapted from ref. [108]

Parameters	SEM	MME
x_1 (nm)	350.1	349.7 ± 0.78
x_2 (nm)	470.9	469.9 ± 0.49
x_3 (°)	86.9	86.9 ± 0.12
x_4 (nm)	39.1	39.1 ± 0.35
x_5 (nm)	–	57.7 ± 2.87
σ_t (nm)	–	3.0 ± 0.57

Figure 25(a) presents the SEM micrograph of another nanoimprinted grating structure, which was imprinted using the same Si imprinting mold. However, due to the process problem when preparing the sample, the nanoimprinted grating structure did not have a symmetric profile. It was known that conventional ellipsometric scatterometry techniques had difficulties in measuring asymmetric grating structures due to the lack of capability in distinguishing the direction of profile asymmetry [113]. In the experiment, it was shown and demonstrated that the Mueller matrix, especially the 2 × 2 off-diagonal blocks of the Mueller matrix, had good sensitivity to both the magnitude and direction of asymmetric profiles [114,115]. We further demonstrated that accurate characterization of asymmetric nanoimprinted gratings can be achieved by performing MME measurements in a conical mounting with the plane of incidence parallel to grating lines (i.e., with $\phi = 90°$) and meanwhile incorporating depolarization effects into the optical model. Figure 25(a) presents the SEM micrograph of the investigated nanoimprinted grating overlaid with the reconstructed structural profile. Figure 25(b) shows the fit results of the measured and calculated best-fit Mueller matrix spectra when taking depolarization effect induced by finite spectral bandwidth and NA into account. Figure 25(c) presents the corresponding DI spectra of the measured and calculated best-fit Mueller matrix spectra.

The sensitivity of the Mueller matrix to both the magnitude and direction of profile asymmetry makes MME well-suited for the measurement of a special kind of structural asymmetry, the overlay. Semiconductor device features are typically patterned layer-by-layer on silicon wafers. These patterns must be aligned accurately, otherwise an overlay error between the top and underlying layers will lead to non-yielding devices. The demand for the tighter overlay control with the ever-decreasing critical dimension poses serious challenges to traditional image-based overlay metrology. The diffraction based overlay (DBO) metrology has now been developed as an important approach to addressing the challenges in overlay monitoring in advanced technology nodes. As a good candidate for DBO metrology, the overlay metrology using MME is based on a property that the elements from the two 2 × 2 off-diagonal blocks of the Mueller matrix are zero when the overlay is absent, otherwise will deviate from zero and respond to the overlay linearly within

a small range [116–118].

The lateral resolution of conventional ellipsometric scatterometry is limited by the illumination spot size, which restricts its application for grating structures located in micro-regions with a smaller size than the illumination spot. In this case, the imaging ellipsometry which is a hybrid of ellipsometry and optical microscopy can be used. Figure 26(a) presents the optical micrograph of pixelated nanogratings used for 3D holographic display. The size of each pixelated grating region is about 100 μm × 100 μm. The grating period and orientation in each pixel are varied to control the direction of emitted light for 3D display. The accurate measurement of the periods, orientations, and structural profiles of the pixelated nanogratings is important to guarantee a good display effect. Figure 26(b) shows the SEM micrograph of one of the pixelated nanogratings overlaid with the adopted geometric model in analysis. Figure 26(c) presents an image of the sample collected by IMME at the wavelength of λ = 630 nm, and Figure 26(d) further shows the corresponding imaging Mueller matrix in the dotted region. With the collected IMME data, we can intuitively choose the interested regions for ellipsometry data analysis. As an example, data analysis was carried out for the point marked with "×" in Figure 26(c). Table 3 presents the comparison of fitting parameters obtained from the IMME and SEM measurements. Figure 27 shows the corresponding fit result of

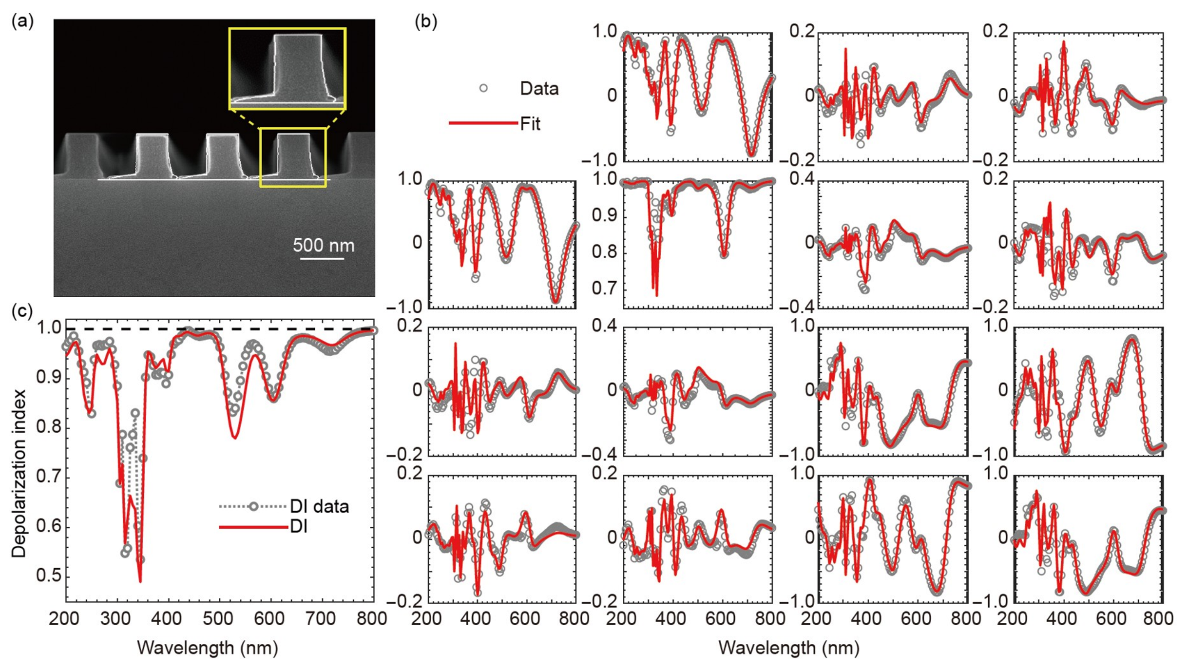

Figure 25 (Color online) (a) SEM micrograph of the nanoimprinted grating structure with the reconstructed profile overlaid; (b) fit result and (c) depolarization index spectra of the measured and calculated best-fit Mueller matrix spectra when considering the depolarization effects induced by finite spectral bandwidth and NA. Data analysis was performed at θ = 65° and ϕ = 90°. The spectral range was varied from 200 to 800 nm with an increment of 5 nm. Adapted from ref. [114].

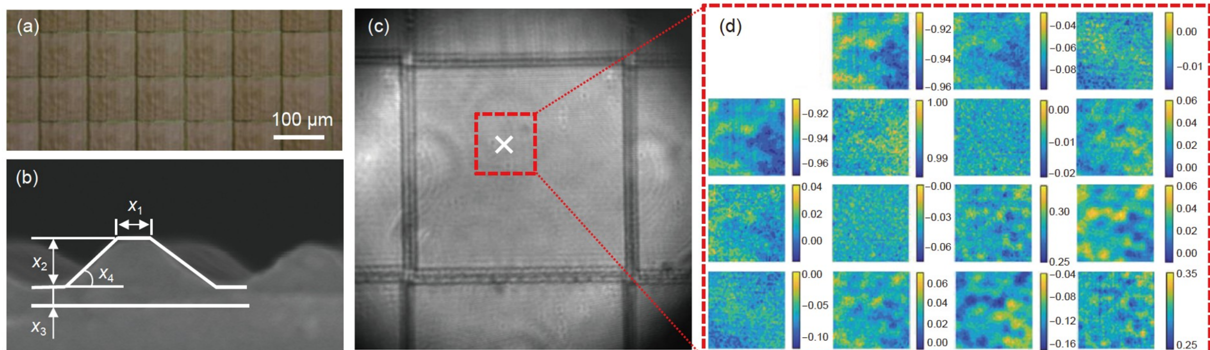

Figure 26 (Color online) (a) Optical micrograph of pixelated nanogratings used for 3D display; (b) SEM micrograph of one of the pixelated nanogratings overlaid with the adopted geometric model in ellipsometry analysis; (c) an image of the investigated sample collected by IMME at λ = 630 nm; (d) the corresponding imaging Mueller matrix in the dotted region shown in Figure 26(c).

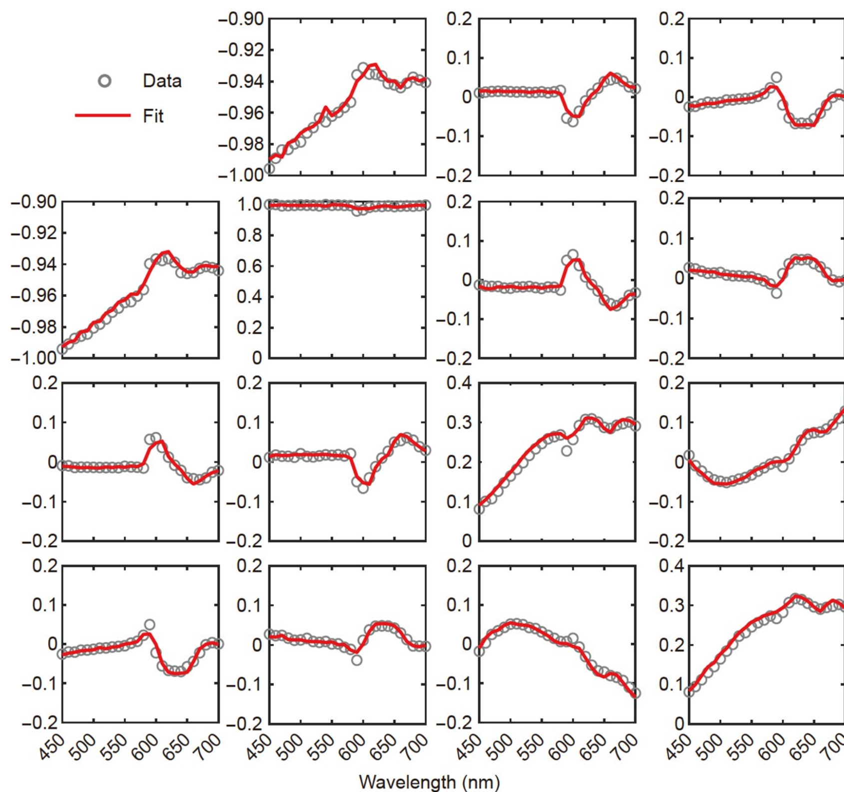

Figure 27 (Color online) Fit result of the IMME-measured and calculated best-fit Mueller matrix spectra corresponding to the point marked with "×" in Figure 26(c).

Table 3 Comparison of fit parameters obtained from IMME and SEM measurements for the point marked with "×" in Figure 26(c). The appended parameter uncertainties correspond to a 95% confidence level

Parameters	Nominal value	SEM	IMME
Period (nm)	530	531	533 ± 3.5
Orientation (°)	10	–	89.5 ± 0.32
x_1 (nm)	–	84.3	83.8 ± 2.25
x_2 (nm)	–	185.4	181.2 ± 4.21
x_3 (nm)	–	–	148.7 ± 3.20
x_4 (°)	–	54.8	50.8 ± 0.89

the measured and calculated best-fit Mueller matrix spectra, from which a good agreement can be observed.

5 Conclusions and perspectives

As a kind of advanced ellipsometry, MME can provide much more information about the sample under test than conventional SE, and thus has drawn great attention since its advent. In the past years, aiming at the instrumentation and emerging applications of advanced ellipsometry, we have developed a broadband MME, which can realize Mueller matrix measurement in a spectral range of 200–1000 nm within about 1 s with a measurement accuracy of better than 0.2% and measurement precision of better than 0.1%. Based on developed MME, we have further developed a high-resolution IMME with a lateral resolution of 0.8 μm and a high-speed MME with a temporal resolution of 11 μs. The developed MMEs have then been applied for the characterization of emerging 2D materials, quasi-1D crystals, organic materials, for the investigation of optical properties of materials in dynamic light-matter interaction, and for the measurement of profiles of subwavelength nanostructures. The applications have demonstrated the great potential of MME.

The ellipsometry analysis typically involves two key issues. One is the instrumentation and another one is the data analysis method. The data analysis in ellipsometry is essentially an inverse problem solving approach, which heavily relies on the prior knowledge of the data analyst. Here, the prior knowledge includes not only the knowledge about the sample under test, but also the professional knowledge about ellipsometry, such as the selection of proper dielectric functions. The professional knowledge about ellipsometry is typically quite challenging for a novice of ellipsometry, which greatly limit the wide applications of ellipsometry in comparison with other characterization tools, such as AFM, SEM, and Raman spectroscopy. So, as for the perspective of advanced ellipsometry, one direction that needs attention is the smart ellipsometry, which could reduce the required prior knowledge in ellipsometry analysis as much as possible,

especially the professional knowledge, by combing with current advanced machine learning methods [119–121].

In addition, the recent years have also witnessed the great progress in metasurfaces and metamaterials. The metasurfaces and metamaterials are artificially structured materials containing sub-wavelength arrays of plasmonic resonators engineered to present optical properties that are usually either difficult or impossible to be obtained in naturally occurring materials and composites. One of the remarkable features of metasurfaces and metamaterials is that they can realize the modulation of several optical properties simultaneously in a compact size, such as polarization modulation and light focusing [122–124]. So, another perspective of advanced ellipsometry would be the instrumentation of compact ellipsometers and even on-chip ellipsometers inspired with results in metasurfaces and metamaterials.

This work was supported by the National Natural Science Foundation of China (Grant Nos. 51727809, 52022034, 62175075, and 52130504), and the Key Research and Development Plan of Hubei Province (Grant Nos. 2020BAA008 and 2021BAA013). The authors would like to thank all the graduate students of Nanoscale and Optical Metrology (NOM) Research Center (http://nom.mse.hust.edu.cn/) for their hard work and contribution during the development and applications of the broadband MME, high-resolution IMME, and high-speed MME.

1 Vedam K. Spectroscopic ellipsometry: A historical overview. Thin Solid Films, 1998, 313-314: 1–9
2 Aspnes D E. Spectroscopic ellipsometry—Past, present, and future. Thin Solid Films, 2014, 571: 334–344
3 Drude P. Ueber die Gesetze der Reflexion und Brechung des Lichtes an der Grenze absorbirender Krystalle. Ann Phys, 1887, 268: 584–625
4 Rothen A. The ellipsometer, an apparatus to measure thicknesses of thin surface films. Rev Sci Instrum, 1945, 16: 26–30
5 Hauge P S. Recent developments in instrumentation in ellipsometry. Surf Sci, 1980, 96: 108–140
6 Azzam R M A, Bashara N M. Ellipsometry and Polarized Light. Amsterdam: North-Holland, 1977
7 Tompkins H K, Irene E A. Handbook of Ellipsometry. New York: Springer, 2005
8 Fujiwara H. Spectroscopic Ellipsometry Principles and Applications. West Sussex: John Wiley & Sons, Ltd., 2007
9 Losurdo M, Hingerl K. Ellipsometry at the Nanoscale. Berlin: Springer, 2013
10 Hinrichs K, Eichhorn K. Ellipsometry of Functional Organic Surfaces and Films. Berlin: Springer, 2014
11 Fujiwara H, Collins R W. Spectroscopic Ellipsometry for Photovoltaics, Volume 1: Fundamental Principles and Solar Cell Characterization. Switzerland: Springer, 2018
12 Azzam R M A. Photopolarimetric measurement of the Mueller matrix by Fourier analysis of a single detected signal. Opt Lett, 1978, 2: 148–150
13 Losurdo M, Bergmair M, Bruno G, et al. Spectroscopic ellipsometry and polarimetry for materials and systems analysis at the nanometer scale: State-of-the-art, potential, and perspectives. J Nanopart Res, 2009, 11: 1521–1554
14 Azzam R M A. Stokes-vector and Mueller-matrix polarimetry. J Opt Soc Am A, 2016, 33: 1396–1408
15 Diebold A C, Antonelli A, Keller N. Perspective: Optical measurement of feature dimensions and shapes by scatterometry. APL Mater, 2018, 6: 058201
16 Arteaga O, Kahr B. Mueller matrix polarimetry of bianisotropic materials. J Opt Soc Am B, 2019, 36: F72
17 Qi J, Elson D S. Mueller polarimetric imaging for surgical and diagnostic applications: A review. J Biophotonics, 2017, 10: 950–982
18 Ramella-Roman J C, Saytashev I, Piccini M. A review of polarization-based imaging technologies for clinical and preclinical applications. J Opt, 2020, 22: 123001
19 He C, He H, Chang J, et al. Polarisation optics for biomedical and clinical applications: A review. Light Sci Appl, 2021, 10: 194
20 Chang C, Chen W, Chen Y, et al. Recent progress on two-dimensional materials. Acta Physico Chim Sin, 2021, 0: 2108017–0
21 Yang F, Cheng S, Zhang X, et al. 2D organic materials for optoelectronic applications. Adv Mater, 2018, 30: 1702415
22 Liu S, Chen X, Zhang C. Development of a broadband Mueller matrix ellipsometer as a powerful tool for nanostructure metrology. Thin Solid Films, 2015, 584: 176–185
23 Chen X, Du W, Yuan K, et al. Development of a spectroscopic Mueller matrix imaging ellipsometer for nanostructure metrology. Rev Sci Instrum, 2016, 87: 053707
24 Chen C, Chen X, Wang C, et al. Imaging Mueller matrix ellipsometry with sub-micron resolution based on back focal plane scanning. Opt Express, 2021, 29: 32712–32727
25 Zhang S, Jiang H, Gu H, et al. High-speed Mueller matrix ellipsometer with microsecond temporal resolution. Opt Express, 2020, 28: 10873–10887
26 Ambirajan A, Look D C. Optimum angles for a polarimeter: Part I. Opt Eng, 1995, 34: 1651–1655
27 Tyo J S. Design of optimal polarimeters: Maximization of signal-to-noise ratio and minimization of systematic error. Appl Opt, 2002, 41: 619–630
28 Smith M H. Optimization of a dual-rotating-retarder Mueller matrix polarimeter. Appl Opt, 2002, 41: 2488–2493
29 Kang T D, Standard E, Carr G L, et al. Rotatable broadband retarders for far-infrared spectroscopic ellipsometry. Thin Solid Films, 2011, 519: 2698–2702
30 Stanislavchuk T N, Kang T D, Rogers P D, et al. Synchrotron radiation-based far-infrared spectroscopic ellipsometer with full Mueller-matrix capability. Rev Sci Instrum, 2013, 84: 023901
31 Garcia-Caurel E, Lizana A, Ndong G, et al. Mid-infrared Mueller ellipsometer with pseudo-achromatic optical elements. Appl Opt, 2015, 54: 2776–2785
32 Feng Y, Huang J, Zhou J, et al. Ultrafast Mueller matrix polarimetry with 10 nanosecond temporal resolution based on optical time-stretch. Opt Lett, 2022, 47: 1403
33 Letnes P A, Nerbø I S, Aas L M S, et al. Fast and optimal broad-band Stokes/Mueller polarimeter design by the use of a genetic algorithm. Opt Express, 2010, 18: 23095–23103
34 Cattelan D, Garcia-Caurel E, Martino A De, et al. Device and method for taking spectroscopic polarimetric measurements in the visible and near-infrared ranges. US Patent, 2011, 0205539 A1
35 Goldstein D H. Mueller matrix dual-rotating retarder polarimeter. Appl Opt, 1992, 31: 6676–6683
36 Collins R W, Koh J. Dual rotating-compensator multichannel ellipsometer: Instrument design for real-time Mueller matrix spectroscopy of surfaces and films. J Opt Soc Am A, 1999, 16: 1997–2006
37 Garcia-Caurel E, De Martino A, Drévillon B. Spectroscopic Mueller polarimeter based on liquid crystal devices. Thin Solid Films, 2004, 455-456: 120–123
38 De Martino A, Kim Y K, Garcia-Caurel E, et al. Optimized Mueller polarimeter with liquid crystals. Opt Lett, 2003, 28: 616–618
39 Aas L M S, Ellingsen P G, Fladmark B E, et al. Overdetermined broadband spectroscopic Mueller matrix polarimeter designed by genetic algorithms. Opt Express, 2013, 21: 8753–8762
40 López-Téllez J M, Bruce N C. Mueller-matrix polarimeter using analysis of the nonlinear voltage-retardance relationship for liquid-

crystal variable retarders. Appl Opt, 2014, 53: 5359
41 Thompson R C, Bottiger J R, Fry E S. Measurement of polarized light interactions via the Mueller matrix. Appl Opt, 1980, 19: 1323–1332
42 Arteaga O, Freudenthal J, Wang B, et al. Mueller matrix polarimetry with four photoelastic modulators: Theory and calibration. Appl Opt, 2012, 51: 6805–6817
43 Oka K, Kato T. Spectroscopic polarimetry with a channeled spectrum. Opt Lett, 1999, 24: 1475–1477
44 Hagen N, Oka K, Dereniak E L. Snapshot Mueller matrix spectropolarimeter. Opt Lett, 2007, 32: 2100–2102
45 Dubreuil M, Rivet S, Le Jeune B, et al. Snapshot Mueller matrix polarimeter by wavelength polarization coding. Opt Express, 2007, 15: 13660–13668
46 Lemaillet P, Rivet S, Le Jeune B. Optimization of a snapshot Mueller matrix polarimeter. Opt Lett, 2008, 33: 144–146
47 Goldstein D H. Polarized Light. 3rd ed. New York: CRC Press, 2011
48 Azzam R M A. Division-of-amplitude photopolarimeter (DOAP) for the simultaneous measurement of all four Stokes parameters of light. Opt Acta-Int J Opt, 1982, 29: 685–689
49 Azzam R M A. Arrangement of four photodetectors for measuring the state of polarization of light. Opt Lett, 1985, 10: 309–311
50 Tripathi S, Toussaint K C. Rapid Mueller matrix polarimetry based on parallelized polarization state generation and detection. Opt Express, 2009, 17: 21396–21407
51 Yeh P. Optical Waves in Layered Media. New York: Wiley-Interscience, 1998
52 Kim H, Park J, Lee B. Fourier Modal Method and its Applications in Computational Nanophotonics. New York: CRC Press, 2012
53 Chen X, Liu S, Zhang C, et al. Improved measurement accuracy in optical scatterometry using correction-based library search. Appl Opt, 2013, 52: 6726–6734
54 Liu S, Chen X, Yang T, et al. Machine learning aided solution to the inverse problem in optical scatterometry. Measurement, 2022, 191: 110811
55 Chen X, Liu S, Gu H, et al. Formulation of error propagation and estimation in grating reconstruction by a dual-rotating compensator Mueller matrix polarimeter. Thin Solid Films, 2014, 571: 653–659
56 Du W, Liu S, Zhang C, et al. Optimal configuration for the dual rotating-compensator Mueller matrix ellipsometer. Proc SPIE, 2013, 8759: 875925
57 Gu H, Chen X, Jiang H, et al. Optimal broadband Mueller matrix ellipsometer using multi-waveplates with flexibly oriented axes. J Opt, 2016, 18: 025702
58 Gu H, Chen X, Jiang H, et al. Accurate alignment of optical axes of a biplate using a spectroscopic Mueller matrix ellipsometer. Appl Opt, 2016, 55: 3935–3941
59 Gu H, Chen X, Shi Y, et al. Comprehensive characterization of a general composite waveplate by spectroscopic Mueller matrix polarimetry. Opt Express, 2018, 26: 25408
60 Gu H, Liu S, Chen X, et al. Calibration of misalignment errors in composite waveplates using Mueller matrix ellipsometry. Appl Opt, 2015, 54: 684–693
61 Gu H, Chen X, Zhang C, et al. Study of the retardance of a birefringent waveplate at tilt incidence by Mueller matrix ellipsometer. J Opt, 2018, 20: 015401
62 Gu H, Chen X, Jiang H, et al. Wide field-of-view angle linear retarder with an ultra-flat retardance response. Opt Lett, 2019, 44: 3026
63 Mishima T, Kao K C. Detection of thickness uniformity of film layers in semiconductor devices by spatially resolved ellipso-interferometry. Opt Eng, 1982, 21: 216074
64 Cohn R F, Wagner J W, Kruger J. Dynamic imaging microellipsometry: Theory, system design, and feasibility demonstration. Appl Opt, 1988, 27: 4664–4671
65 Erman M, Theeten J B. Spatially resolved ellipsometry. J Appl Phys, 1986, 60: 859–873
66 Beaglehole D. Performance of a microscopic imaging ellipsometer. Rev Sci Instrum, 1988, 59: 2557–2559
67 Jin G, Jansson R, Arwin H. Imaging ellipsometry revisited: Developments for visualization of thin transparent layers on silicon substrates. Rev Sci Instrum, 1996, 67: 2930–2936
68 Laude-Boulesteix B, De Martino A, Drévillon B, et al. Mueller polarimetric imaging system with liquid crystals. Appl Opt, 2004, 43: 2824–2832
69 Arteaga O, Baldrís M, Antó J, et al. Mueller matrix microscope with a dual continuous rotating compensator setup and digital demodulation. Appl Opt, 2014, 53: 2236–2245
70 Liu S, Du W, Chen X, et al. Mueller matrix imaging ellipsometry for nanostructure metrology. Opt Express, 2015, 23: 17316–17329
71 Tan Y, Chen C, Chen X, et al. Development of a tomographic Mueller-matrix scatterometer for nanostructure metrology. Rev Sci Instrum, 2018, 89: 073702
72 Chen C, Chen X, Gu H, et al. Calibration of polarization effect of a high-numerical-aperture objective lens with Mueller matrix polarimetry. Meas Sci Technol, 2019, 30: 025201
73 Sheng S, Chen X, Chen C, et al. Eigenvalue calibration method for dual rotating-compensator Mueller matrix polarimetry. Opt Lett, 2021, 46: 4618–4621
74 Jellison G E, Modine F A. Two-modulator generalized ellipsometry: Theory. Appl Opt, 1997, 36: 8190–8198
75 Liu J, Zhang C, Zhong Z, et al. Measurement configuration optimization for dynamic metrology using Stokes polarimetry. Meas Sci Technol, 2018, 29: 054010
76 Zhang S, Wang L, Yi A, et al. Dynamic modulation performance of ferroelectric liquid crystal polarization rotators and Mueller matrix polarimeter optimization. Front Mech Eng, 2020, 15: 256–264
77 Zhang S, Gu H, Liu J, et al. Characterization of beam splitters in the calibration of a six-channel Stokes polarimeter. J Opt, 2018, 20: 125606
78 Gu H, Zhu S, Song B, et al. An analytical method to determine the complex refractive index of an ultra-thin film by ellipsometry. Appl Surf Sci, 2020, 507: 145091
79 Song B, Gu H, Zhu S, et al. Broadband optical properties of graphene and HOPG investigated by spectroscopic Mueller matrix ellipsometry. Appl Surf Sci, 2018, 439: 1079–1087
80 Fang M, Gu H, Song B, et al. Thickness and layer stacking order effects on complex optical conductivity and exciton strength of few-layer graphene: Implications for optical modulators and photodetectors. ACS Appl Nano Mater, 2022, 5: 1864–1872
81 Song B, Gu H, Fang M, et al. Layer-dependent dielectric function of wafer-scale 2D MoS_2. Adv Opt Mater, 2019, 7: 1801250
82 Song B, Gu H, Fang M, et al. Complex optical conductivity of two-dimensional MoS_2: A striking layer dependency. J Phys Chem Lett, 2019, 10: 6246–6252
83 Gu H, Song B, Fang M, et al. Layer-dependent dielectric and optical properties of centimeter-scale 2D WSe_2: Evolution from a single layer to few layers. Nanoscale, 2019, 11: 22762–22771
84 Song B, Gu H, Fang M, et al. 2D niobium-doped MoS_2: Tuning the exciton transitions and potential applications. ACS Appl Electron Mater, 2021, 3: 2564–2572
85 Fang M, Gu H, Song B, et al. Thickness scaling effects on the complex optical conductivity of few-layer WSe_2 investigated by spectroscopic ellipsometry. Adv Photon Res, 2022, 3: 2100299
86 Fang M, Wang Z, Gu H, et al. Layer-dependent dielectric permittivity of topological insulator Bi_2Se_3 thin films. Appl Surf Sci, 2020, 509: 144822
87 Fang M, Wang Z, Gu H, et al. Complex optical conductivity of Bi_2Se_3 thin film: Approaching two-dimensional limit. Appl Phys Lett, 2021, 118: 191101
88 Song B, Hou J, Wang H, et al. Determination of dielectric functions and exciton oscillator strength of two-dimensional hybrid perovskites. ACS Mater Lett, 2021, 3: 148–159
89 Guo Z, Gu H, Fang M, et al. Complete dielectric tensor and giant optical anisotropy in quasi-one-dimensional $ZrTe_5$. ACS Mater Lett,

2021, 3: 525–534
90 Hou S, Guo Z, Yang J, et al. Birefringence and dichroism in quasi-1D transition metal trichalcogenides: Direct experimental investigation. Small, 2021, 17: 2100457
91 Yu Y, Xiong T, Guo Z, et al. Wide-spectrum polarization-sensitive and fast-response photodetector based on 2D group IV-VI semiconductor tin selenide. Fundamental Res, 2022, doi: 10.1016/j.fmre.2022.02.008
92 Song B, Liu F, Wang H, et al. Giant gate-tunability of complex refractive index in semiconducting carbon nanotubes. ACS Photon, 2020, 7: 2896–2905
93 Xia R, Gu H, Liu S, et al. Optical analysis for semitransparent organic solar cells. Sol RRL, 2019, 3: 1800270
94 Zhang K, Fan B, Xia R, et al. Highly efficient tandem organic solar cell enabled by environmentally friendly solvent processed polymeric interconnecting layer. Adv Energy Mater, 2018, 8: 1703180
95 Ding K, Fang Y, Dong S, et al. 24.1% external quantum efficiency of flexible quantum dot light-emitting diodes by light extraction of silver nanowire transparent electrodes. Adv Opt Mater, 2018, 6: 1800347
96 Xiang S, Lv X, Sun S, et al. To improve the efficiency of thermally activated delayed fluorescence OLEDs by controlling the horizontal orientation through optimizing stereoscopic and linear structures of indolocarbazole isomers. J Mater Chem C, 2018, 6: 5812–5820
97 Zhao X, Xia R, Gu H, et al. Performance optimization of tandem organic solar cells at varying incident angles based on optical analysis method. Opt Express, 2020, 28: 2381–2397
98 Zhao X, Gu H, Chen L, et al. Optical model and optimization for coherent-incoherent hybrid organic solar cells with nanostructures. Nanomaterials, 2022, 11: 3187
99 Ke X, Gu H, Zhao X, et al. Simulation method for study on outcoupling characteristics of stratified anisotropic OLEDs. Opt Express, 2019, 27: A1014
100 Ke X, Gu H, Chen L, et al. Multi-objective collaborative optimization strategy for efficiency and chromaticity of stratified OLEDs based on an optical simulation method and sensitivity analysis. Opt Express, 2020, 28: 27532–27546
101 Ali S J, Bolme C A, Collins G W, et al. Development of a broadband reflectivity diagnostic for laser driven shock compression experiments. Rev Sci Instrum, 2015, 86: 043112
102 Pust N J, Shaw J A. Dual-field imaging polarimeter using liquid crystal variable retarders. Appl Opt, 2006, 45: 5470–5478
103 Zhang S, Chen C, Jiang H, et al. Dynamic characteristics of nematic liquid crystal variable retarders investigated by a high-speed polarimetry. J Opt, 2019, 21: 065605
104 Wei P, Gu H, Chen X, et al. Characterization of a liquid crystal variable retarder by Mueller matrix ellipsometry. Proc SPIE, 2019, 11053: 110531Q
105 Bueno J M. Polarimetry using liquid-crystal variable retarders: theory and calibration. J Opt A-Pure Appl Opt, 2000, 2: 216–222
106 Hilfiker J N, Herzinger C M, Wagner T, et al. Mueller-matrix characterization of liquid crystals. Thin Solid Films, 2004, 455-456: 591–595
107 Chen X, Zhang C, Liu S. Depolarization effects from nanoimprinted grating structures as measured by Mueller matrix polarimetry. Appl Phys Lett, 2013, 103: 151605
108 Chen X, Liu S, Zhang C, et al. Accurate characterization of nanoimprinted resist patterns using Mueller matrix ellipsometry. Opt Express, 2014, 22: 15165–15177
109 Novikova T, De Martino A, Ben Hatit S, et al. Application of Mueller polarimetry in conical diffraction for critical dimension measurements in microelectronics. Appl Opt, 2006, 45: 3688–3697
110 Chen X, Liu S, Zhang C, et al. Measurement configuration optimization for accurate grating reconstruction by Mueller matrix polarimetry. J Micro Nanolith MEMS MOEMS, 2013, 12: 033013
111 Dong Z, Liu S, Chen X, et al. Determination of an optimal measurement configuration in optical scatterometry using global sensitivity analysis. Thin Solid Films, 2014, 562: 16–23
112 Chen X, Gu H, Jiang H, et al. Probing optimal measurement configuration for optical scatterometry by the multi-objective genetic algorithm. Meas Sci Technol, 2018, 29: 045014
113 Novikova T, De Martino A, Ossikovski R, et al. Metrological applications of Mueller polarimetry in conical diffraction for overlay characterization in microelectronics. Eur Phys J Appl Phys, 2005, 31: 63–69
114 Chen X, Zhang C, Liu S, et al. Mueller matrix ellipsometric detection of profile asymmetry in nanoimprinted grating structures. J Appl Phys, 2014, 116: 194305
115 Chen X, Jiang H, Zhang C, et al. Towards understanding the detection of profile asymmetry from Mueller matrix differential decomposition. J Appl Phys, 2015, 118: 225308
116 Kim Y N, Paek J S, Rabello S, et al. Device based in-chip critical dimension and overlay metrology. Opt Express, 2009, 17: 21336–21343
117 Li J, Liu Y, Dasari P, et al. Advanced diffraction-based overlay for double patterning. Proc SPIE, 2010, 7638: 76382C
118 Chen X, Gu H, Jiang H, et al. Robust overlay metrology with differential Mueller matrix calculus. Opt Express, 2017, 25: 8491–8510
119 Liu J, Zhang D, Yu D, et al. Machine learning powered ellipsometry. Light Sci Appl, 2021, 10: 55
120 Oiwake K, Nishigaki Y, Fujimoto S, et al. Fully automated spectroscopic ellipsometry analyses: Application to MoO_x thin films. J Appl Phys, 2021, 129: 243102
121 Arunachalam A, Berriel S N, Feit C, et al. Machine learning approach to thickness prediction from *in situ* spectroscopic ellipsometry data for atomic layer deposition processes. J Vacuum Sci Tech A, 2022, 40: 012405
122 Balthasar Mueller J P, Leosson K, Capasso F. Ultracompact metasurface in-line polarimeter. Optica, 2016, 3: 42–47
123 Rubin N A, D'Aversa G, Chevalier P, et al. Matrix Fourier optics enables a compact full-Stokes polarization camera. Science, 2019, 365: eaax1839
124 Dorrah A H, Rubin N A, Zaidi A, et al. Metasurface optics for on-demand polarization transformations along the optical path. Nat Photon, 2021, 15: 287–296